Progress Report on the Analysis of Jet Engine Inlets

H.T. Anastasiu, D.C. Ross and J.L. Volakis

Wright Laboratories/AARA
Wright Patterson AFB,
Ohio 45433-7001
Dayton, OH 45431

Veda, Inc.
Suite 200
5200 Springfield Pike

July 1994

30395-5-T = RL-2420

030395-5-T

Progress Report on the Analysis of Jet Engine Inlets

H. Anastassiu, D. Ross and J.L. Volakis

Radiation Laboratory
Electrical Engineering and Computer Science Dept.
University of Michigan
Ann Arbor, MI 48109-2122

July 1994

Background and Executive Summary

The University of Michigan activity on the electromagnetic characterization of jet engine inlets began in January 1993 with the goal of developing robust hybrid methods for the electromagnetic analysis of cavities terminated with jet engines, i.e. cavities terminated with an array of blades which normally form the compressor of the engine configuration. Since high frequency techniques cannot be used for the characterization of the complex engine face, our method of analysis called for a hybrid approach. Specifically, we proposed to use a numerical method for modeling the engine face and a well known high frequency method for propagating the fields to and from the engine face. Among some of the obvious challenges to be confronted in this implementation were

- Large Computational Domains (actual engine is 10-50λ in diameter).
- Complexity of the Engine Face.
- Lack of Experience in Interfacing a Numerical and High Frequency Methods.
- Lack of Validation/Reference Data.

Thus, it was obvious from the start of this analysis that a simplified computational model had to be developed for a characterization of practical jet engine configurations. Nevertheless, confronted with no physical insight on the reflectivity of realistic jet engines, we began with the development of a rigorous hybrid finite element-modal method (FEM-Modal). In parallel with this effort, a more traditional mode matching approach was used for the analysis of a few canonical configurations. The purpose of this analysis was to develop reference data to validate the rigorous FEM-Modal approach. Below we summarize our progress and different stages of our study. We discuss the developed codes as well as their capabilities and accuracy. Also, future work is outlined. The reader is referred to the main body of this report and the previous progress reports of this activity for a more detailed account.

- **Hybrid Finite Element Code Development**

The development of this code began last year as the first rigorous attempt for a characterization of the jet engine scattering. As noted above, this hybrid technique utilizes the FEM to model the engine and a ray/modal method to trace the fields from the engine mouth to the engine face and back. More recently, a similar hybrid FD-TD technique is being developed at Ohio State. However, as usual the FD-TD is limited in geometrical adaptability unless excessive zoning is imposed. In the case of blade modeling, the FEM offers unique advantages in its geometrical adaptability and field representation.

The first three dimensional FEM code was completed at the end of January 1994 and this code was validated using a number of benchmark geometries. As part of this code, we developed a new artificial absorber for terminating the finite element mesh and several difficulties had to be overcome as relates to the element selection, system stability, imposition of the boundary conditions, geometry data preprocessing, data rendition and so on.

Nevertheless, it became apparent during the development of this hybrid FEM code that the simulation of realistic jet engines would require excessive computation time without using special techniques aimed at reducing the CPU requirements. With this in mind we began looking at a number of ways for the purpose of developing a practical code which can be interfaced with XPATCH. The proposed generalized transmission line formulation is began as an alternative approach which holds a great promise in developing a practical code, albeit approximate. However, our search of ways to speed-up the FEM code was also very fruitful. Specifically, we found that in modeling the engine, only a single blade need be modeled. This approach is very similar to that used for the analysis of Bodies of Revolution(BOR) and its implementation consumed our effort since the early part of this year(FY94). As is well known, in the case of BORs the incident field is decomposed into modes and for each mode the 3D problem is reduced to an equivalent 2D problem. Thus, the computational demands are reduced from those of a 3D problem to those of a 2D problem. The only drawback is that the "2D" analysis must be repeated for each mode. However, this is required for the generation of the scattering matrix.

The formulation for slicing the computational domain is described in this report and a code has been implemented on the basis of this formulation. Perhaps the most troublesome part of this implementation dealt with the periodic boundary conditions which must be imposed across a three dimensional boundary outlining the starting and ending surface of a single periodic cell comprising the compressor. This was overcome but required a rather involved implementation. As of the moment only preliminary results have been generated which prove the validity of the model.

A most important outcome of the periodic FEM formulation is the realization that in the case of engine terminations comprised of many blades (positioned symmetrically around the stator), there is very limited mode coupling as explained in this report. That is, the incoming mode couples only to a few (known apriori) modes and this can be exploited to further reduce the computational demands of the FEM-Modal solution. Moreover, it can be used to develop a simplified model for computing the scattering by engine terminations. It should be also remarked that the limited mode coupling had already been observed in our earlier scattering matrices but to date no rigorous proof was available (see main body of the report). It is certainly our intent to fully exploit the simplifications resulting from this observation.

The following summarizes the status of the FEM-Modal code development

- Completed and validated the first FEM-Modal code.
  Code incorporates special artificial absorber for terminating the mesh; Uses nodal elements; Accepts actual geometry in facets or other curvilinear patches; Generates scattering matrix; Can be readily interfaced with any high frequency method; Has been validated; Does not exploit engine's periodicity and does not take advantage of limited mode coupling; Requires 20,000 unknowns per unit volume and its application is consequently limited to small cavities.

- Developed a new FEM-Modal formulation and associated code which exploits symmetry and mode periodicity.
  Implementation employs new phase boundary conditions; Only one slice (volume between blades) need be modeled, thus

reducing the CPU demand by a factor of N_s=number of blades; Limited mode coupling identifies important modes apriori leading to additional computational efficiencies; Preliminary validation has been completed.

- Future work will concentrate on developing FEM-Modal formulation using solution-aware basis.

- **Generalized Telegraphist Equation-Mode Matching Method (GTE-MM Method)**

As mentioned above, in parallel with the rigorous FEM-Modal formulation and code development, we also proceeded with the development of analysis codes specialized to specific canonical but engine-like configurations. Indeed, codes were developed for the analysis of two reference configurations as discussed in the report. These configurations proved quite important since they provided to the entire community reference data for validating the various approximate and rigorous codes under development.

However, the most important outcome of this effort was the realization that the modes guided by a pair of engine-like curved blades can be described in analytic form. This can be done via the generalized Telegraphist equation(GTE) method as described in the report. The development and use of the GTE for this application was of great importance because it opened the way to construct an approximate but simple, efficient and sufficiently accurate mode matching(MM) code for the analysis of jet engines. Since the early part of this year, we have proceeded to develop of a GTE-MM code with the goal of interfacing this code with ray techniques. As of this moment, the status of the GTE-MM is as follows:

- Developed a GTE-MM code for a single-stage compressor Back face of compressor can be characterized by another scattering matrix; Code was shown to reduce to the relevant canonical configuration; Limited validation because of lack of reference data. Code was written to utilize minimum resources; Code is simple and has been successfully run for up to 5λ radius inlets. Larger geometries do not pose a major computational challenge.

- Generalized single stage GTE-MM code to multiple compressor stages. Code involves several small matrix inversions. Generated results and compared them with the GO1 measured data; Agreement was quite reasonable given the difference between the measurement and computational model, as well as the uncertainties associated with the measured data.

- Future work will concentrate on:
  Further validation and optimization of the GTE-MM code.
  Exploitation of limited mode coupling to reduce matrix size and CPU requirements

The Mode Matching Technique for Electromagnetic Scattering by an Approximate Model of a Jet Engine Inlet.

Hristos T. Anastassiu John L. Volakis

July 1994

Abstract

The Mode Matching Technique is applied to the evaluation of the Radar Cross-Section of cylindrical inlets which include multiple stages of curved blades mounted on a perfectly conducting cylindrical hub. The wave propagation in the grooves formed by the curved blades is analyzed via generalized transmission line theory. The model closely approximates the structure of a realistic jet engine inlet. The numerical results yield an approximate value of the Radar Cross-Section of a realistic engine inlet, and they can also be used as a reference solution for the validation of codes based on more versatile numerical techniques, such as the Finite Element Method.

1 Introduction

In a previous report [1] we used the Mode-Matching Technique to compute the Radar Cross-Section (RCS) of cylindrical inlets with two different kinds of terminations. Initially we investigated the case of a perfectly conducting cylindrical hub placed on a flat metal plate which terminates the inlet. Furthermore, we mounted an array of sectoral metal blades on the hub and performed the same analytical techniques to evaluate the RCS of the new geometry. Numerical results showed good comparison with other methods and direct measurements.

In reality, though, any jet engine has very few (if any) blades with planar boundary surfaces. Usually the blades are curved in a complicated manner which makes the rigorous analysis of the geometry very difficult, if not impossible. In this report we will show how the problem can be solved in a formally exact way, provided that some conditions hold true. The electromagnetic propagation in the vicinity of the curved blades is analyzed via generalized modes in the context of the Generalized Telegraphist's Equations method (G.T.E.). The conventional Mode Matching Technique is somewhat modified so that it can handle these generalized modes. The RCS of the

cavity is evaluated in a way identical to [1].

Moreover, in this report we will show how to apply the results of our Mode Matching technique to inlets with multiple stages. We will show that in such a geometry it is straightforward to evaluate the overall modal scattering matrix in a recursive manner, starting from the termination and moving backwards to the open end. This allows a successive evaluation of the scattering matrices which correspond to the interfaces between the various sections. The algorithm is fairly general, and it can be applied to any geometry where either conventional or generalized modes can be defined.

A code has been written on the basis of the G.T.E. method and the cascading scheme to analyze multiple compressor stages. Because of the G.T.E. method used in representing the fields between compressor blades, it is expected that the code will handle geometries which closely resemble actual engine configurations. Preliminary results are presented which show reasonable agreement with the measured data of the GO1 model. However, more accurate data are necessary for an acceptable validation of the multiple stages code.

2 Propagation Inside an Array of Curved Blades

In [1] we dealt exclusively with a special class of termination geometries. None of these represents a realistic jet inlet, but nevertheless they proved useful for validating other techniques, such as the Finite Element and Finite Difference methods, applied to the same problem. With the goal of characterizing the scattering of more realistic jet inlet terminations, in this report we present a mode matching solution for an inlet termination consisting of a special class of curved blades.

We can conceptualize the curved blades geometry as a generalization, or perturbation of that shown in fig. 1. Let us assume that the array of straight blades in these figures consists of J grooves, which are essentially cylindrical (pie-shell) sectors. We shall also assume, without loss of generality, that the rightmost edge of the first groove makes an angle ϕ_1 with the x-axis, and consequently, the rightmost edge of the κth groove will form the angle

$$\phi_\kappa = \phi_1 + (\kappa - 1)\frac{2\pi}{J} \tag{1}$$

with the x-axis, where ϕ_w is the angular extent of each groove. The fields in

the κth groove are explicitly given in Appendix I (also see [1]).

To obtain a more reasonable model for the curved blades structure we opt to modify the geometry in fig. 1. Basically, each blade is allowed to be curved with the restriction that its base still remains perpendicular to the hub at any point of intersection (see fig. 2) However, the angle formed by the rightmost edge of the boundary of the blade and the x-axis is allowed to vary. Specifically the blade or the groove boundary is now allowed to make an angle

$$\phi_\kappa(z) = \phi_1 + (\kappa - 1)\frac{2\pi}{J} + F(z) \tag{2}$$

with the x axis, where F is an arbitrary function of the longitudinal coordinate z (it is essentially a variable angle measured in radians). If z_0 is the location of the face of the fan, obviously the condition

$$F(z_0) = 0 \tag{3}$$

should be satisfied, so that at the face of the fan

$$\phi_1(z_0) = \phi_1 \tag{4}$$

Note that (2) is valid provided all blades have the same z-dependence, resulting in grooves of constant width for any z; that is each pair of blades is assumed to form an identical guiding region as in the case in practice.

Our goal is to modify the exact solution of the straight blade geometry to help us analyze the curved blade geometry. This is feasible since the two geometries share some common characteristics. For any given z the cross-section of any curved blade pair is identical to that of a straight blade pair, with the only difference being the rotation about the z axis. Obviously, the modes described in Appendix I (eq. (25)-(28)) still satisfy the appropriate boundary conditions, provided ϕ_κ satisfies (2). It is therefore safe to assume that the transverse fields within the κth groove (i.e. the waveguide region between the $(\kappa-1)^{th}$ and the κth blades) can be expressed as a superposition of the aforementioned generalized modes, i.e.

$$\mathbf{E}_\kappa^t = \sum_{i=1}^{\infty} V_{\kappa,i}(z)\mathbf{e}_{\kappa,i}(\rho,\phi;z) \tag{5}$$

$$\mathbf{H}_\kappa^t = \sum_{i=1}^{\infty} I_{\kappa,i}(z)\mathbf{h}_{\kappa,i}(\rho,\phi;z) \tag{6}$$

It can be shown [2] that the coefficients $V_{\kappa,i}(z), I_{\kappa,i}(z)$ satisfy the following infinite system of differential equations:

$$\frac{d}{dz}\begin{Bmatrix} V_{\kappa,1}(z) \\ V_{\kappa,2}(z) \\ \dots \\ I_{\kappa,1}(z) \\ I_{\kappa,2}(z) \\ \dots \end{Bmatrix} = \begin{bmatrix} T_{11}(z) & T_{12}(z) & \dots & -j\beta_1 Z_1 & 0 & \dots \\ T_{21}(z) & T_{22}(z) & \dots & 0 & -j\beta_2 Z_2 & \dots \\ \dots & \dots & \dots & \dots & \dots & \dots \\ -\frac{j\beta_1}{Z_1} & 0 & \dots & -T_{11}(z) & -T_{21}(z) & \dots \\ 0 & -\frac{j\beta_2}{Z_2} & \dots & -T_{12}(z) & -T_{22}(z) & \dots \\ \dots & \dots & \dots & \dots & \dots & \dots \end{bmatrix} \begin{Bmatrix} V_{\kappa,1}(z) \\ V_{\kappa,2}(z) \\ \dots \\ I_{\kappa,1}(z) \\ I_{\kappa,2}(z) \\ \dots \end{Bmatrix} \tag{7}$$

where

$$T_{ij}(z) \equiv \int\int_{S_\kappa(z)} \mathbf{e}_{\kappa,j} \cdot \frac{\partial \mathbf{e}_{\kappa,i}}{\partial z} d^2S \tag{8}$$

β_i is the propagation constant, z_i is the impedance of the ith mode and $S_\kappa(z)$ is the cross-section of the κth groove at z. Given $F(z)$, analytical evaluation of $\frac{\partial \mathbf{e}_{\kappa,i}}{\partial z}$ is feasible. In (8) the ϕ integration can be performed in closed form, but the ρ integration has to be performed numerically.

Under some assumptions, system (7) can be solved in closed form. Since the cross-section of all grooves remains invariant in shape along the axis, the propagation constants and the impedances of the modes do not depend on the longitudinal coordinate z. Therefore, eq. (7) can be written in the following compact form:

$$\frac{d}{dz}\{\mathbf{U}_\kappa(z)\} = [\mathbf{M}(z)]\{\mathbf{U}_\kappa(z)\} \tag{9}$$

where

$$\{\mathbf{U}_\kappa(z)\} \equiv \left\{ \begin{array}{c} V_{\kappa,1}(z) \\ V_{\kappa,2}(z) \\ \cdots \\ Z_1 I_{\kappa,1}(z) \\ Z_2 I_{\kappa,2}(z) \\ \cdots \end{array} \right\} \tag{10}$$

$$[\mathbf{M}(z)] \equiv \left[\begin{array}{cc} [\mathbf{P}]\, F'(z) & [\mathbf{D}] \\ [\mathbf{D}] & -[\mathbf{P}]^T F'(z) \end{array} \right] \tag{11}$$

$$[\mathbf{D}] = \mathbf{diag}[-j\beta_1, -j\beta_2 ...] \tag{12}$$

and

$$P_{ij} \equiv -\int\int_{S_\kappa(z)} \mathbf{e}_{\kappa,j} \cdot \frac{\partial \mathbf{e}_{\kappa,i}}{\partial \phi_\kappa} d^2 S \tag{13}$$

Given the explicit expressions of $\mathbf{e}_{\kappa,i}$ in Appendix I, it is obvious that P_{ij} does not depend on z. We observe in (11) that the dependence of [M] on z is due to the presence of $F'(z)$, that is if $F'(z)$ is a constant, [M] becomes independent of z and this can be exploited to obtain a closed form solution of $\{\mathbf{U}_\kappa(z)\}$. Specifically, it follows that if $F(z)$ is linear, the explicit solution for $\{\mathbf{U}_\kappa(z)\}$ is

$$\{\mathbf{U}_\kappa(z)\} = \exp(z[\mathbf{M}])\{\mathbf{U}_\kappa(0)\} \tag{14}$$

where $\{\mathbf{U}_\kappa(0)\}$ is the value at $z = 0$. Although this is an explicit solution, the numerical evaluation of the matrix exponential is not an easy task. The standard approach is to find the eigenvalues and eigenvectors of [M]. If λ_i are the eigenvalues and [K] is the matrix of the eigenvectors, then

$$e^{z[\mathbf{M}]} = [\mathbf{K}]\,\mathbf{diag}\left[e^{z\lambda_1}, e^{z\lambda_2}, ..., e^{z\lambda_n}\right][\mathbf{K}]^{-1} \tag{15}$$

In theory, matrix [M] is infinite, but for numerical purposes one has to truncate it, taking into account only the traveling and the most significant evanescent modes. Since the available techniques for the evaluation of the eigenvalues of general, full matrices are not reliable for very large dimensions of the matrix, it is evident that the truncated matrix must be reasonably small. Moreover, an additional problem of instability occurs due to the existence of eigenvalues with vary large real parts (in absolute value). This problem is easily overcome, due to the following property of matrix [M] (see Appendix II for the proof):

If λ is an eigenvalue of [M], $-\lambda$ is also an eigenvalue of [M].

This is an expected property, since within each guided region identical paired modes should propagate along the $+z$ and the $-z$ directions. Also, due to this property, the eigenvalues of $[\mathbf{M}]$ can be seperated into two sets and the solution to (7) can be written as

$$\left\{ \begin{array}{c} \mathbf{V}_\kappa(z) \\ \mathbf{I}_\kappa(z) \end{array} \right\} = \left[\begin{array}{cc} [\mathbf{K}_{11}] & [\mathbf{K}_{12}] \\ [\mathbf{K}_{21}] & [\mathbf{K}_{22}] \end{array} \right] \left[\begin{array}{cc} e^{[\Lambda]z} & \mathbf{0} \\ \mathbf{0} & e^{-[\Lambda]z} \end{array} \right] \left[\begin{array}{cc} [\mathbf{K}_{11}] & [\mathbf{K}_{12}] \\ [\mathbf{K}_{21}] & [\mathbf{K}_{22}] \end{array} \right]^{-1} \left\{ \begin{array}{c} \mathbf{V}_\kappa(0) \\ \mathbf{I}_\kappa(0) \end{array} \right\} \tag{16}$$

where

$$[\Lambda] \equiv \mathbf{diag}\,[\lambda_1, ..., \lambda_\rho] \tag{17}$$

$$Re(\lambda) \;>\; 0 \text{ or} \tag{18}$$

$$Re(\lambda) \;=\; 0, Im(\lambda) \geq 0 \tag{19}$$

The impedances $Z_{\kappa,i}$ have been incorporated to the current functions $I_{\kappa,i}$.

Expression (16) is very helpful in applying the Mode-Matching technique to the geometry. Following the analysis in Appendix III, the scattering matrix of the compressor at its interface with the hollow portion of the cylinder is derived to be

$$[\mathbf{S}] = ([\mathbf{W}] + [\mathbf{I}])^{-1} ([\mathbf{W}] - [\mathbf{I}]) \tag{20}$$

where

$$[\mathbf{W}] = \sum_{\kappa=1}^{J} [\mathbf{L}_\kappa]^T [\mathbf{F}_\kappa] [\mathbf{G}_\kappa]^{-1} [\mathbf{L}_\kappa] \tag{21}$$

$[\mathbf{I}]$ is the unit matrix,

$$[\mathbf{F}_\kappa] \equiv [\mathbf{K}_{11}] + [\mathbf{K}_{12}] [\mathbf{R}_\kappa] \tag{22}$$

$$[\mathbf{G}_\kappa] \equiv [\mathbf{K}_{21}] + [\mathbf{K}_{22}] [\mathbf{R}_\kappa] \tag{23}$$

$$[\mathbf{R}_\kappa] \equiv e^{-[\mathbf{\Lambda}]l} [\mathbf{K}_{12}]^{-1} [\mathbf{S}_{0,\kappa}] [\mathbf{K}_{11}] e^{-[\mathbf{\Lambda}]l} \tag{24}$$

$[\mathbf{S}_{0,\kappa}]$ is the scattering matrix of the termination of the κth groove, l is the length of the compressor and $[\mathbf{L}_\kappa]$ is the matrix which represents the coupling among the modes of the two regions of the inlet (for the explicit definition of $[\mathbf{L}_\kappa]$ see Appendix III). It is evident that since the real part of the elements of $[\mathbf{\Lambda}]$ are chosen to be nonnegative, (an immediate consequence of the aforementioned property concerning the eigenvalues of $[\mathbf{M}]$), no numerical instabilities occur. Finally, it is straightforward to show that the above expressions reduce to those for the straight blades (see Appendix IV for proof).

The case of the straight blades corresponds to setting $F(z) = constant$. Of course, the only allowable constant is 0, due to (3).

3 Numerical Results for a Circular Inlet Terminated by a Cylindrical Array of Curved Blades

In fig. 3 and 4 we present numerical results for the RCS of an inlet terminated by an array of curved blades. For the results in these figures the outer radius of the inlet is $b = \lambda$, the hub radius is $a = 0.5\lambda$, the length of the first (hollow) region is $l_1 = 5\lambda$ and the length of the fan is $l_2 = \lambda$. Also, there are 4 blades attached to the hub, the angular width of each groove is $\phi_w = 80^o$ and the angular location of the first groove is $\phi_1 = 0$. Three separate plots are presented for each polarization: the solid line corresponds to straight blades (no twist angle); the dotted line corresponds to a total twist angle of 10° and the dashed line to a total twist angle of 30°. Note that in this case "twist angle" denotes the value of $F(z)$ at the back end of the fan.

4 Cascaded Configuration

The expressions developed so far dealt with the simple geometry of a circular cylinder terminated by a single compressor stage, consisting of an array of blades. Nevertheless, they are in a rather general form and this permits us to extend them into inlets terminated by multiple sections, as illustrated in in fig. 5. To analyze this geometry, we start from the last termination and then successively compute in a recursive way the scattering matrices relevant to each interface. Specifically, using the termination scattering matrix and the formulas developed either in this report or in [1] (according to the geometry), we compute the scattering matrix at interface $n-1$. The latter scattering matrix plays the role of the "termination" matrix for region $n-2$. Therefore, following the same procedure, we evaluate the scattering matrix at inteface $n-2$ and so on, until we finally reach the open end. The RCS is calculated by the standard procedure described in [1].

5 Numerical Results for the Cascade Configuration

Numerical results for the cascade configuration were compared to measurements of the GO1 engine model taken at the Ohio State University [3]. The

geometry of the GO1 model is depicted in fig. 6, 7, 8. Two configurations were tested. The short version had the engine directly connected to the inlet (fig. 7), while the long version had a hollow cylinder (see fig. 8) between the engine and the inlet. Measurements were taken at 2, 3 and 4 GHz. The model for the Mode Matching cascade code is depicted in fig. 9. Only two stages were taken into account, and the diameter of the cylindrical hub in the computational model was set equal to the average diameter of the GO1 hub. Point L′ corresponds to the median of L and K in the GO1 geometry, i.e. its distance from the nose of the engine (point M) is equal to the average distance of L and K from the same point. Furthermore, point J′ is the median of J and I, point H′ is the median of H and G and point F′ is the median of F and E. The model was backed by a perfectly conducting lid. The blades were all straight. In the first stage (region L′J′), the width of each blade was equal to 1.54° while in the second stage (region H′F′) each blade had a width of 1.85°. In the mathematical model, unlike the GO1, all blades were assumed to touch the inner surface of the duct.

Comparisons between measurements and numerical results are shown in figs. 10-13. Given the different geometrical characteristics of the mathematical model and the GO1 structure, the agreement is considered satisfactory at

this preliminary stage. One should take in account the fact that the relative positions of the blades in the GO1 model were not known when the measurements were taken. An arbitrary relative position was used in the numerical results. Also, part of the disagreement is due to the hub scattering. As shown in fig. 6, the hub of the GO1 model was tapered to a tip, whereas in the computational model the hub was abruptly truncated causing additional scattering.

6 Summary and Conclusion

In this report we have used the Mode Matching Technique in conjunction with the G.T.E. for the characterization of configurations which closely resemble realistic jet engine inlets. We found a closed form solution for the wave propagation between the curved compressor blades and the Mode Matching technique was employed to obtain the mode scattering matrix. The latter was used to evaluate the RCS of a cylindrical cavity terminated by a class of engine compressors. The method was also generalized to handle multiple stages of compressors. A computer code was developed to generate the mode scattering matrix of single and multiple stage compressors situated in a cylindrical inlet. The results generated by this code were compared with

corresponding data based on a Finite Element and Finite Difference methods. Since these methods can only handle small size inlets, we had to resort to the limited measured data available at this time. Specifically, our calculations via the G.T.E. - M.M. method were compared with the the measured RCS data of the GO1 model collected at Ohio State [3]. Although the GO1 geometry was not precisely that of the calculation model, fairly good agreement was observed and this is a preliminary demonstration of the code's accuracy and capability. Nevertheless, better measurements and better testing is required.

7 Appendix I: Explicit Analytical Expressions for the Modes within the Termination:

Region 2, κ^{th} groove (groove array termination).

$$
\begin{aligned}
\mathbf{e}_{2,\kappa,mq}^{TM} &= \gamma_{2,mq}^{TM}\left[Y_\nu\left(\gamma_{2,mq}^{TM}a\right)J_\nu'\left(\gamma_{2,mq}^{TM}\rho\right)-J_\nu\left(\gamma_{2,mq}^{TM}a\right)Y_\nu'\left(\gamma_{2,mq}^{TM}\rho\right)\right]\cdot \\
&\cdot\ N_{2,mq}^{TM}\frac{\beta_{2,mq}^{TM}}{\omega\epsilon}\sin\left[\nu\left(\phi-\phi_\kappa\right)\right]\mathbf{u}_\rho + \\
&+\ \frac{\nu}{\rho}\left[Y_\nu\left(\gamma_{2,mq}^{TM}a\right)J_\nu\left(\gamma_{2,mq}^{TM}\rho\right)-J_\nu\left(\gamma_{2,mq}^{TM}a\right)Y_\nu\left(\gamma_{2,mq}^{TM}\rho\right)\right]\cdot \\
&\cdot\ N_{2,mq}^{TM}\frac{\beta_{2,mq}^{TM}}{\omega\epsilon}\cos\left[\nu\left(\phi-\phi_\kappa\right)\right]\mathbf{u}_\phi
\end{aligned}
\tag{25}
$$

$$
\begin{aligned}
\mathbf{h}_{2,\kappa,mq}^{TM} &= \frac{\nu}{\rho}\left[Y_\nu\left(\gamma_{2,mq}^{TM}a\right)J_\nu\left(\gamma_{2,mq}^{TM}\rho\right)-J_\nu\left(\gamma_{2,mq}^{TM}a\right)Y_\nu\left(\gamma_{2,mq}^{TM}\rho\right)\right]\cdot \\
&\cdot\ N_{2,mq}^{TM}\cos\left[\nu\left(\phi-\phi_\kappa\right)\right]\mathbf{u}_\rho - \\
&- \gamma_{2,mq}^{TM}\left[Y_\nu\left(\gamma_{2,mq}^{TM}a\right)J_\nu'\left(\gamma_{2,mq}^{TM}\rho\right)-J_\nu\left(\gamma_{2,mq}^{TM}a\right)Y_\nu'\left(\gamma_{2,mq}^{TM}\rho\right)\right]\cdot \\
&\cdot\ N_{2,mq}^{TM}\sin\left[\nu\left(\phi-\phi_\kappa\right)\right]\mathbf{u}_\phi \qquad (26)
\end{aligned}
$$

$$
\begin{aligned}
\mathbf{e}_{2,\kappa,mq}^{TE} &= \frac{\nu}{\rho}\left[Y_\nu'\left(\gamma_{2,mq}^{TE}a\right)J_\nu\left(\gamma_{2,mq}^{TE}\rho\right)-J_\nu'\left(\gamma_{2,mq}^{TE}a\right)Y_\nu\left(\gamma_{2,mq}^{TE}\rho\right)\right]\cdot \\
&\cdot\ N_{2,mq}^{TE}\sin\left[\nu\left(\phi-\phi_\kappa\right)\right]\mathbf{u}_\rho + \\
&+ \gamma_{2,mq}^{TE}\left[Y_\nu'\left(\gamma_{2,mq}^{TE}a\right)J_\nu'\left(\gamma_{2,mq}^{TE}\rho\right)-J_\nu'\left(\gamma_{2,mq}^{TE}a\right)Y_\nu'\left(\gamma_{2,mq}^{TE}\rho\right)\right]\cdot \\
&\cdot\ N_{2,mq}^{TE}\cos\left[\nu\left(\phi-\phi_\kappa\right)\right]\mathbf{u}_\phi \qquad (27)
\end{aligned}
$$

$$
\begin{aligned}
\mathbf{h}_{2,\kappa,mq}^{TE} &= \gamma_{2,mq}^{TE}\left[Y_\nu'\left(\gamma_{2,mq}^{TE}a\right)J_\nu'\left(\gamma_{2,mq}^{TE}\rho\right)-J_\nu'\left(\gamma_{2,mq}^{TE}a\right)Y_\nu'\left(\gamma_{2,mq}^{TE}\rho\right)\right]\cdot \\
&\cdot\ N_{2,mq}^{TE}\frac{\beta_{2,mq}^{TE}}{\omega\mu}\cos\left[\nu\left(\phi-\phi_\kappa\right)\right]\mathbf{u}_\rho - \\
&- \frac{\nu}{\rho}\left[Y_\nu'\left(\gamma_{2,mq}^{TE}a\right)J_\nu\left(\gamma_{2,mq}^{TE}\rho\right)-J_\nu'\left(\gamma_{2,mq}^{TE}a\right)Y_\nu\left(\gamma_{2,mq}^{TE}\rho\right)\right]\cdot \\
&\cdot\ N_{2,mq}^{TE}\frac{\beta_{2,mq}^{TE}}{\omega\mu}\sin\left[\nu\left(\phi-\phi_\kappa\right)\right]\mathbf{u}_\phi \qquad (28)
\end{aligned}
$$

where

$$
J_\nu(\gamma_{mq}^{TM}a)Y_\nu(\gamma_{mq}^{TM}b)-J_\nu(\gamma_{mq}^{TM}b)Y_\nu(\gamma_{mq}^{TM}a)=0 \qquad (29)
$$

$$
J_\nu'(\gamma_{mq}^{TE}a)Y_\nu'(\gamma_{mq}^{TE}b)-J_\nu'(\gamma_{mq}^{TE}b)Y_\nu'(\gamma_{mq}^{TE}a)=0 \qquad (30)
$$

and

$$\nu = \frac{m\pi}{\phi_w}, \qquad m \in \mathbf{N}_0 \tag{31}$$

$$N_{2,mq}^{TM} \equiv -\frac{\omega\epsilon}{\beta_{2,mq}^{TM}}\frac{1}{2}\sqrt{\frac{\phi_w(3-\epsilon_m)}{2}}\left[\frac{J_\nu^2\left(\gamma_{2,mq}^{TM}a\right)}{J_\nu^2\left(\gamma_{2,mq}^{TM}b\right)}-1\right]^{-\frac{1}{2}} \tag{32}$$

$$N_{2,mq}^{TE} \equiv \frac{1}{2}\sqrt{\frac{\phi_w(3-\epsilon_m)}{2}}\left\{\left[\frac{J_\nu'\left(\gamma_{2,mq}^{TE}a\right)}{J_\nu'\left(\gamma_{2,mq}^{TE}b\right)}\right]^2\left[1-\left(\frac{\nu}{\gamma_{2,mq}^{TE}b}\right)^2\right]-\right.$$
$$\left.-\left[1-\left(\frac{\nu}{\gamma_{2,mq}^{TE}a}\right)^2\right]\right\}^{-\frac{1}{2}} \tag{33}$$

$$\epsilon_m \equiv \begin{cases} 2 & m=0 \\ 1 & m\neq 0 \end{cases} \tag{34}$$

8 Appendix II: The Eigenvalue Symmetry Property of the G.T.E. Matrix

The following property holds for matrix [M] of eq. (11):

If λ is an eigenvalue of [M], $-\lambda$ is also an eigenvalue of [M].

The proof is based on the three following Lemmata:

Lemma 1: For any matrix $[\mathbf{A}]$, $\det[\mathbf{A}] = \det\left[\mathbf{A}^T\right]$

(Proof well-known)

Lemma 2: Let $[\mathbf{A}_{ij}]$ be $n \times n$ complex matrices. Then

$$\begin{vmatrix} [\mathbf{A}_{11}] & [\mathbf{A}_{12}] \\ [\mathbf{A}_{21}] & [\mathbf{A}_{22}] \end{vmatrix} = \begin{vmatrix} [\mathbf{A}_{11}] & -[\mathbf{A}_{12}] \\ -[\mathbf{A}_{21}] & [\mathbf{A}_{22}] \end{vmatrix} \tag{35}$$

Proof: Let [I] be the $n \times n$ unit matrix. Evidently

$$\begin{bmatrix} [\mathbf{A}_{11}] & -[\mathbf{A}_{12}] \\ -[\mathbf{A}_{21}] & [\mathbf{A}_{22}] \end{bmatrix} = \begin{bmatrix} [\mathbf{I}] & [\mathbf{0}] \\ [\mathbf{0}] & -[\mathbf{I}] \end{bmatrix} \begin{bmatrix} [\mathbf{A}_{11}] & [\mathbf{A}_{12}] \\ [\mathbf{A}_{21}] & [\mathbf{A}_{22}] \end{bmatrix} \begin{bmatrix} [\mathbf{I}] & [\mathbf{0}] \\ [\mathbf{0}] & -[\mathbf{I}] \end{bmatrix} \tag{36}$$

Given that

$$\begin{vmatrix} [\mathbf{I}] & [\mathbf{0}] \\ [\mathbf{0}] & -[\mathbf{I}] \end{vmatrix} = \pm 1 \tag{37}$$

and that the determinant of a product of matrices is equal to the product of their determinants, the proof of the lemma is obvious.

Lemma 3: Let [A], [B], [C] be $n \times n$ complex matrices. Then

$$\begin{vmatrix} [\mathbf{A}] & [\mathbf{C}] \\ [\mathbf{C}] & [\mathbf{B}] \end{vmatrix} = \begin{vmatrix} [\mathbf{B}] & [\mathbf{C}] \\ [\mathbf{C}] & [\mathbf{A}] \end{vmatrix} \tag{38}$$

Proof: Similar to Lemma 2. Note that

$$\begin{bmatrix} [\mathbf{B}] & [\mathbf{C}] \\ [\mathbf{C}] & [\mathbf{A}] \end{bmatrix} = \begin{bmatrix} [\mathbf{0}] & [\mathbf{I}] \\ [\mathbf{I}] & [\mathbf{0}] \end{bmatrix} \begin{bmatrix} [\mathbf{A}] & [\mathbf{C}] \\ [\mathbf{C}] & [\mathbf{B}] \end{bmatrix} \begin{bmatrix} [\mathbf{0}] & [\mathbf{I}] \\ [\mathbf{I}] & [\mathbf{0}] \end{bmatrix} \tag{39}$$

and consequently (38) holds since

$$\begin{vmatrix} [\mathbf{0}] & [\mathbf{I}] \\ [\mathbf{I}] & [\mathbf{0}] \end{vmatrix} = \pm 1 \tag{40}$$

and since the determinant of a product of matrices is equal to the product of their determinants.

Using the above three Lemmata, we can develop the proof of the eigenvalue symmetry property as follows:

Proof of the Eigenvalue Symmetry Property:

Let

$$[\mathbf{M}] \equiv \begin{bmatrix} [\mathbf{A}] & [\mathbf{D}] \\ [\mathbf{D}] & -[\mathbf{A}]^T \end{bmatrix} \tag{41}$$

where $[\mathbf{D}]$ is a diagonal matrix. If λ be an eigenvalue of $[\mathbf{M}]$, then by definition

$$\begin{vmatrix} [\mathbf{A}] - \lambda\,[\mathbf{I}] & [\mathbf{D}] \\ [\mathbf{D}] & -[\mathbf{A}]^T - \lambda\,[\mathbf{I}] \end{vmatrix} = 0 \tag{42}$$

Further, by using Lemma 1, and since $[\mathbf{D}]$ is diagonal, we have

$$\begin{vmatrix} [\mathbf{A}]^T - \lambda\,[\mathbf{I}] & [\mathbf{D}] \\ [\mathbf{D}] & -[\mathbf{A}] - \lambda\,[\mathbf{I}] \end{vmatrix} = 0 \tag{43}$$

or, equivalently

$$\begin{vmatrix} -[\mathbf{A}]^T + \lambda\,[\mathbf{I}] & -[\mathbf{D}] \\ -[\mathbf{D}] & [\mathbf{A}] + \lambda\,[\mathbf{I}] \end{vmatrix} = 0 \tag{44}$$

Next, from Lemma 2, (44) yields

$$\begin{vmatrix} -[\mathbf{A}]^T + \lambda\,[\mathbf{I}] & [\mathbf{D}] \\ [\mathbf{D}] & [\mathbf{A}] + \lambda\,[\mathbf{I}] \end{vmatrix} = 0 \tag{45}$$

and finally Lemma 3 gives

$$\begin{vmatrix} [\mathbf{A}] + \lambda\,[\mathbf{I}] & [\mathbf{D}] \\ [\mathbf{D}] & -[\mathbf{A}]^T + \lambda\,[\mathbf{I}] \end{vmatrix} = 0 \tag{46}$$

This result shows that $-\lambda$ is an eigenvalue of [M], Q.E.D.

9 Appendix III: Application of the Mode Matching Technique to the Generalized Modes within the Compressor

In this section we apply the Mode Matching Technique to the geometry of Fig. 2 in order to evaluate the scattering matrix of the curved blades array.

In Region 1 the transverse fields are given as a superposition of cylindrical waveguide modes [1]:

$$\mathbf{E}_1^t = \sum_{p=1}^{\infty} [a_p \mathbf{e}_{1,p} \exp\{j\beta_{1,p} z\} + b_p \mathbf{e}_{1,p} \exp\{-j\beta_{1,p} z\}] \tag{47}$$

$$\mathbf{H}_1^t = \sum_{p=1}^{\infty} [a_p \mathbf{h}_{1,p} \exp\{j\beta_{1,p} z\} + b_p \mathbf{h}_{1,p} \exp\{-j\beta_{1,p} z\}] \tag{48}$$

where a_p, b_p are the coefficients of the incident and the reflected fields due to the termination. Similarly, according to (6) the transverse fields in the κth of region 2 are expressed as superpositions of the generalized modes:

$$\mathbf{E}^t_{2,\kappa} = \sum_{i=1}^{\infty} V_{\kappa,i}(z)\mathbf{e}_{2,\kappa,i}(\rho,\phi;z) \tag{49}$$

$$\mathbf{H}^t_{2,\kappa} = \sum_{i=1}^{\infty} I_{\kappa,i}(z)\mathbf{h}_{2,\kappa,i}(\rho,\phi;z) \tag{50}$$

From (16) we deduce that in the κth groove

$$\{\mathbf{V}_\kappa\} = [\mathbf{K}_{11}]\,\mathrm{e}^{z[\mathbf{\Lambda}]}\{\mathbf{c}_\kappa\} + [\mathbf{K}_{12}]\,\mathrm{e}^{-z[\mathbf{\Lambda}]}\{\mathbf{d}_\kappa\} \tag{51}$$

$$\{\mathbf{I}_\kappa\} = [\mathbf{K}_{21}]\,\mathrm{e}^{z[\mathbf{\Lambda}]}\{\mathbf{c}_\kappa\} + [\mathbf{K}_{22}]\,\mathrm{e}^{-z[\mathbf{\Lambda}]}\{\mathbf{d}_\kappa\} \tag{52}$$

where $\{\mathbf{c}_\kappa\}$, $\{\mathbf{d}_\kappa\}$ are vectors of arbitrary constants.

To evaluate $\{\mathbf{b}\} \equiv \{b_1, b_2, ...\}^T$ in terms of $\{\mathbf{a}\} \equiv \{a_1, a_2, ...\}^T$ we must impose the continuity of the tangential fields at the interface. Furthermore, the tangential electric fields must vanish on any PEC surfaces.

Let us locate the origin of the coordinate system at the interface between the two regions. Enforcing continuity of the tangential electric field at the interface yields

$$\mathbf{E}^t_1|_{z=0} = \mathbf{E}^t_2|_{z=0} \tag{53}$$

$$\mathbf{H}^t_1|_{z=0} = \mathbf{H}^t_2|_{z=0} \tag{54}$$

$$\forall \rho \in [a,b], \forall \phi \in [\phi_\kappa(0), \phi_\kappa(0) + \phi_w], \forall \kappa \in \{1, ..., J\}$$

On combining (53) with (47) and (49), taking the dot product with the modes $\mathbf{e}_{1,q}$ and integrating over the whole interface, we obtain the system

$$[\mathbf{U}](\{\mathbf{a}\} + \{\mathbf{b}\}) = \sum_{\kappa=1}^{J} [\mathbf{M}_\kappa]([\mathbf{K}_{11}]\{\mathbf{c}_\kappa\} + [\mathbf{K}_{12}]\{\mathbf{d}_\kappa\}) \tag{55}$$

where

$$M_{\kappa,qp} \equiv \int_a^b \int_{\phi_\kappa}^{\phi_\kappa+\phi_w} \mathbf{e}_{2,\kappa,q} \cdot \mathbf{e}_{1,p} \rho d\rho d\phi \tag{56}$$

$$U_{mn} \equiv \delta_{mn} \int_0^b \int_0^{2\pi} \mathbf{e}_{1,m} \cdot \mathbf{e}_{1,n} \rho d\rho d\phi \tag{57}$$

and δ_{mn} is the Kronecker delta.

In a similar way, on combining (54) with (48) and (50), taking the dot product with the modes $\mathbf{h}_{2,\kappa,q}$ and integrating over the portion of the interface common to both regions, we obtain the system

$$[\mathbf{Q}_\kappa](\{\mathbf{a}\} - \{\mathbf{b}\}) = [\mathbf{V}_\kappa]([\mathbf{K}_{21}]\{\mathbf{c}_\kappa\} + [\mathbf{K}_{22}]\{\mathbf{d}_\kappa\}) \ \forall \kappa = 1, ..., J \tag{58}$$

where

$$Q_{\kappa,qp} \equiv \int_a^b \int_{\phi_\kappa}^{\phi_\kappa+\phi_w} \mathbf{h}_{2,\kappa,q} \cdot \mathbf{h}_{1,p} \rho d\rho d\phi \tag{59}$$

$$V_{mn} \equiv \delta_{mn} \int_a^b \int_0^{2\pi} \mathbf{h}_{2,m} \cdot \mathbf{h}_{2,n} \rho d\rho d\phi \tag{60}$$

and δ_{mn} is the Kronecker delta.

If $[\mathbf{S}_{0,\kappa}]$ is the scattering matrix of the termination corresponding to the κth groove, then, by definition,

$$[\mathbf{K}_{12}]\, e^{l_2[\Lambda]} \{\mathbf{d}_\kappa\} = [\mathbf{S}_{0,\kappa}]\, [\mathbf{K}_{11}]\, e^{-l_2[\Lambda]} \{\mathbf{c}_\kappa\} \tag{61}$$

where l_2 is the length of the second region. Expression (61) provides a relation between $\{\mathbf{c}_\kappa\}$ and $\{\mathbf{d}_\kappa\}$. To find $\{\mathbf{b}_\kappa\}$ we must solve systems (55), (58) and (61). Obviously, $\{\mathbf{b}_\kappa\}$ will be a function of $\{\mathbf{a}_\kappa\}$, and to avoid repeating the solution for every excitation, it is customary to instead compute the scattering matrix $[\mathbf{S}]$ defined by

$$\{\mathbf{b}_\kappa\} = [\mathbf{S}]\, \{\mathbf{a}_\kappa\} \tag{62}$$

To help define the scattering matrix, we introduce some auxilliary definitions:

$$[\mathbf{R}_\kappa] \equiv e^{-[\Lambda]l_2}\, [\mathbf{K}_{12}]^{-1}\, [\mathbf{S}_{0,\kappa}]\, [\mathbf{K}_{11}]\, e^{-[\Lambda]l_2} \tag{63}$$

$$[\mathbf{F}_\kappa] \equiv [\mathbf{K}_{11}] + [\mathbf{K}_{12}]\,[\mathbf{R}_\kappa] \tag{64}$$

$$[\mathbf{G}_\kappa] \equiv [\mathbf{K}_{21}] + [\mathbf{K}_{22}]\,[\mathbf{R}_\kappa] \tag{65}$$

$$[\mathbf{L}_\kappa] \equiv [\mathbf{V}_\kappa]^{-1}\,[\mathbf{Q}_\kappa] \tag{66}$$

Then, from (55), (58), (61) and (62) it follows that

$$[\mathbf{S}] = ([\mathbf{W}] + [\mathbf{I}])^{-1}\,([\mathbf{W}] - [\mathbf{I}]) \tag{67}$$

where

$$[\mathbf{W}] = \sum_{\kappa=1}^{J} [\mathbf{L}_\kappa]^T\,[\mathbf{F}_\kappa]\,[\mathbf{G}_\kappa]^{-1}\,[\mathbf{L}_\kappa] \tag{68}$$

and $[\mathbf{I}]$ is the unit matrix.

10 Appendix IV: The Exponential Matrix Solution of the Generalized Telegraphists Equations.

In this Appendix we give an explicit form of the matrix exponential appearing in (14) when the blades are straight. It is shown that the well-known solution of the conventional Telegraphist's Equations is recovered.

In the case of straight blades, $F'(z) = 0$. Hence

$$[\mathbf{M}] = \begin{bmatrix} [\mathbf{0}] & [\mathbf{D}] \\ [\mathbf{D}] & [\mathbf{0}] \end{bmatrix} \tag{69}$$

One observes that

$$[\mathbf{M}]^2 = \begin{bmatrix} [\mathbf{D}]^2 & [\mathbf{0}] \\ [\mathbf{0}] & [\mathbf{D}]^2 \end{bmatrix} = [\mathbf{Q}]^2 \tag{70}$$

where

$$[\mathbf{Q}] = \begin{bmatrix} [\mathbf{D}] & [\mathbf{0}] \\ [\mathbf{0}] & [\mathbf{D}] \end{bmatrix} \tag{71}$$

Thus

$$\begin{aligned}
\exp[\mathbf{M}] &= [\mathbf{I}] + [\mathbf{M}] + \frac{1}{2!}[\mathbf{M}]^2 + \frac{1}{3!}[\mathbf{M}]^3 + \ldots \\
&= \left\{[\mathbf{I}] + \frac{1}{2!}[\mathbf{M}]^2 + \frac{1}{4!}[\mathbf{M}]^4 + \ldots\right\} + \left\{[\mathbf{M}] + \frac{1}{3!}[\mathbf{M}]^3 + \frac{1}{5!}[\mathbf{M}]^5 + \ldots\right\} \\
&= \left\{[\mathbf{I}] + \frac{1}{2!}[\mathbf{Q}]^2 + \frac{1}{4!}[\mathbf{Q}]^4 + \ldots\right\} + [\mathbf{M}]\left\{[\mathbf{Q}] + \frac{1}{3!}[\mathbf{Q}]^3 + \frac{1}{5!}[\mathbf{Q}]^5 + \ldots\right\}[\mathbf{Q}]^{-1} \\
&= \cosh[\mathbf{Q}] + [\mathbf{M}]\sinh[\mathbf{Q}][\mathbf{Q}]^{-1} \\
&= \begin{bmatrix} \cosh[\mathbf{D}] & \sinh[\mathbf{D}] \\ \sinh[\mathbf{D}] & \cosh[\mathbf{D}] \end{bmatrix}
\end{aligned} \tag{72}$$

The latter equation, in conjunction with (10) and (16) yields

$$V_{\kappa,i} = c_{\kappa,i}e^{j\beta_i z} + d_{\kappa,i}e^{-j\beta_i z} \tag{73}$$

$$Z_0 I_{\kappa,i} = c_{\kappa,i}e^{j\beta_i z} - d_{\kappa,i}e^{-j\beta_i z} \tag{74}$$

where

$$c_{\kappa,i} \equiv \frac{1}{2}\left[V_{\kappa,i}(0) + Z_0 I_{\kappa,i}(0)\right] \tag{75}$$

$$d_{\kappa,i} \equiv \frac{1}{2}\left[V_{\kappa,i}(0) - Z_0 I_{\kappa,i}(0)\right] \tag{76}$$

This is the well-known solution of the conventional Telegraphist's Equations.

References

[1] H. T. Anastassiu and J. L. Volakis, "The Mode Matching Technique for Electromagnetic Scattering by Inlets with Complex Terminations", Technical Report 030395-3-T, The University of Michigan, EECS Radiation Laboratory, Ann Arbor MI, October 1993.

[2] G. Reiter, "Generalized Telegraphist's Equation for Waveguides of Varying Cross-Section", *Proc. I.E.E.* vol. 106B, suppl. 13, pp. 54-57, 1959.

[3] A. Dominek et al., personal communication.

LIST OF FIGURES:

Figure 1: Cylindrical inlet terminated by an array of straight blades.

Figure 2: Cylindrical inlet terminated by an array of curved blades.

Figure 3: RCS (dB/λ^2) calculated by the G.T.E. - M. M. technique for a curved blade termination with $a = 0.5\lambda, b = \lambda, l_1 = 5\lambda, l_2 = \lambda, 4$ fins, $\phi_1 = 0^o$. (θ polarization).

Figure 4: RCS (dB/λ^2) calculated by the G.T.E. - M. M. technique for a curved blade termination with $a = 0.5\lambda, b = \lambda, l_1 = 5\lambda, l_2 = \lambda, 4$ fins, $\phi_1 = 0^o$. (ϕ polarization).

Figure 5: Illustration of a cavity with multiple sections having different propagation characteristics.

Figure 6: Some dimensions of the GO1 model.

Figure 7: The short version of the GO1 measurement configuration.

Figure 8: The duct inserted between the engine and the inlet to construct the long version of the GO1 measurement configuration.

Figure 9: Computational model of the GO1 (2 stages).

Figure 10. Comparison between numerical results (solid line) and measurements (dotted line) for the GO1 short inlet model (2 GHz, θ polarization).

Figure 11. Comparison between numerical results (solid line) and mea-

surements (dotted line) for the GO1 short inlet model (2 GHz, ϕ polarization).

Figure 12. Comparison between numerical results (solid line) and measurements (dotted line) for the GO1 short inlet model (3 GHz, θ polarization).

Figure 13. Comparison between numerical results (solid line) and measurements (dotted line) for the GO1 short inlet model (3 GHz, ϕ polarization).

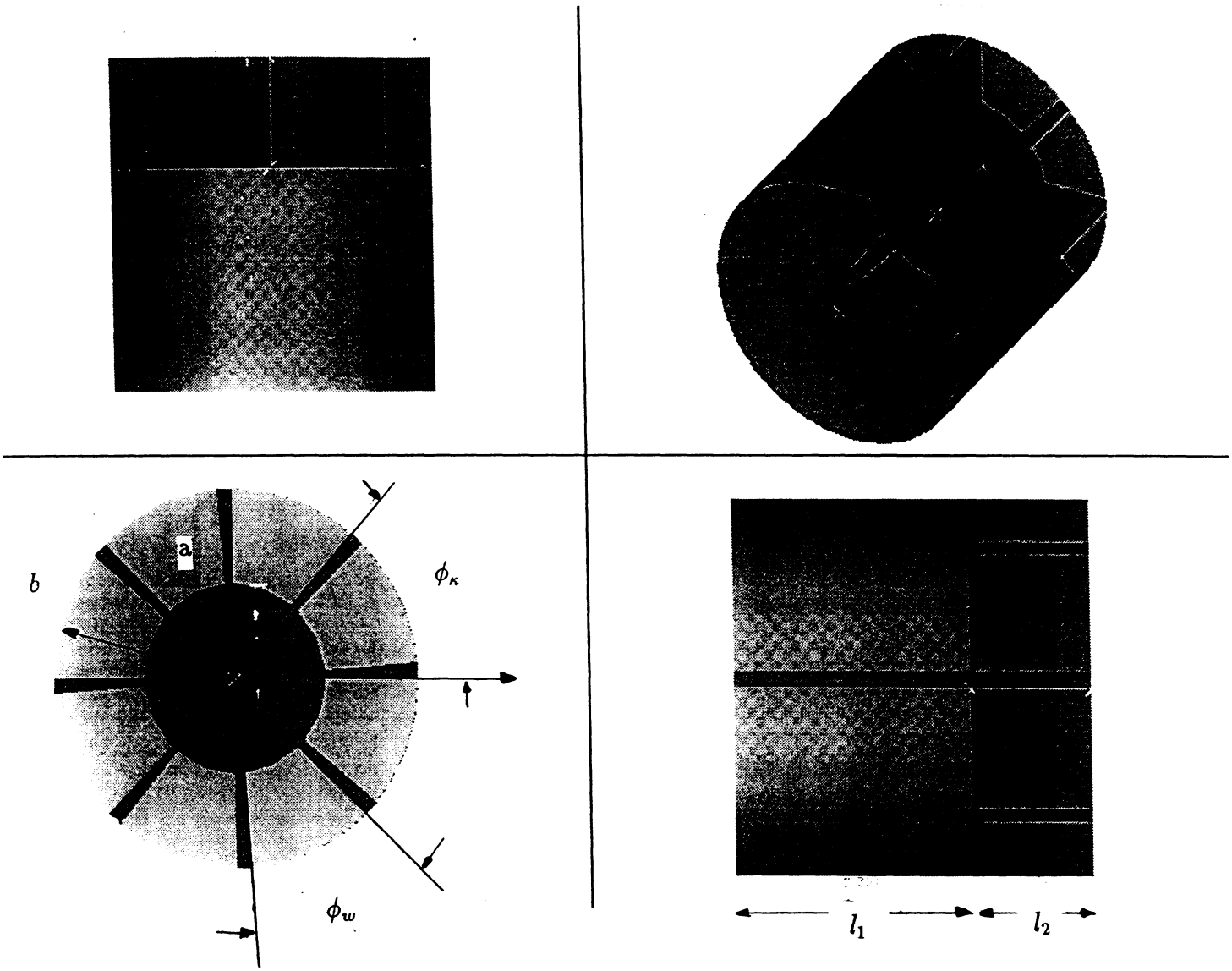

Figure 1: Cylindrical inlet terminated by an array of straight blades.

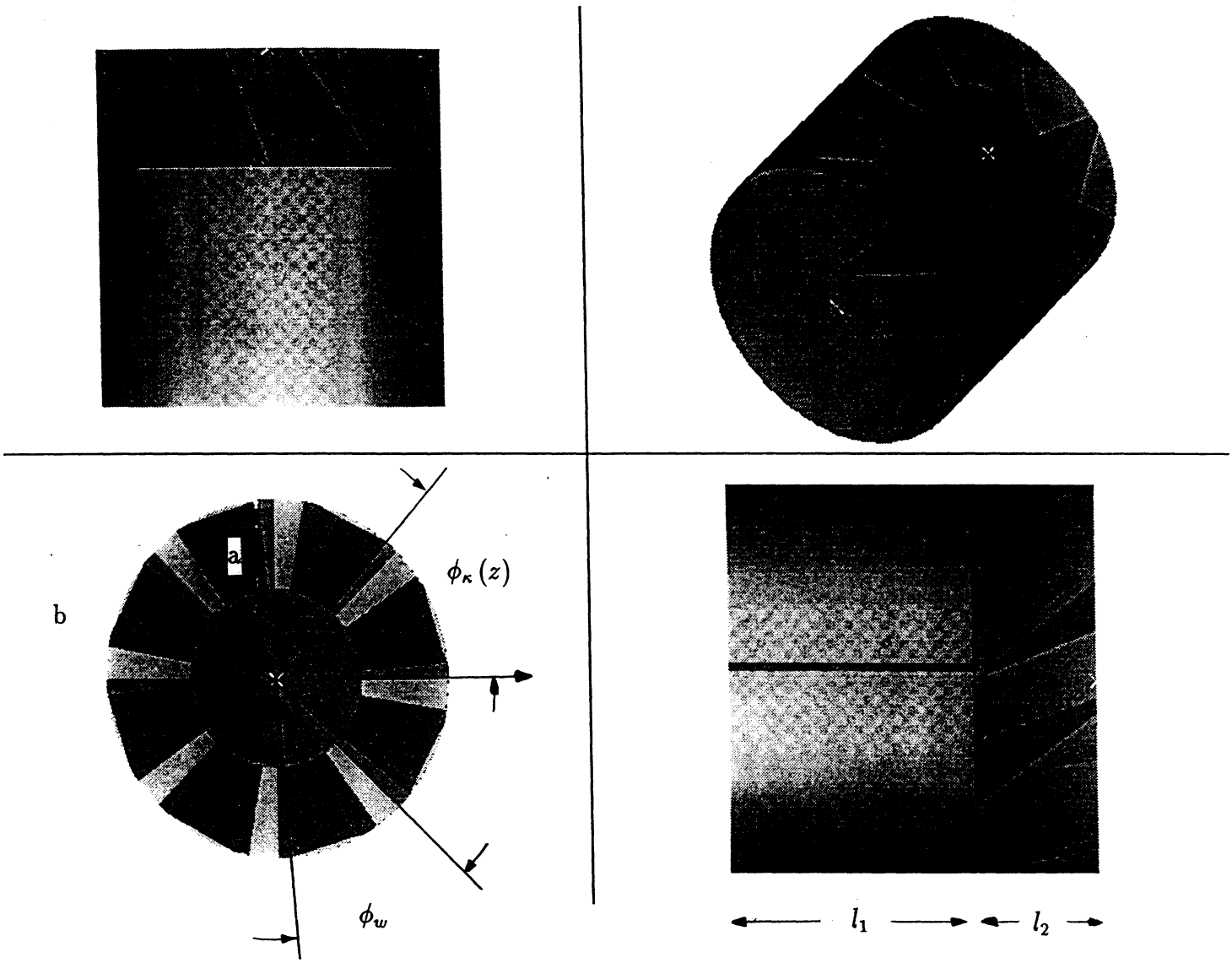

Figure 2: Cylindrical inlet terminated by an array of curved blades.

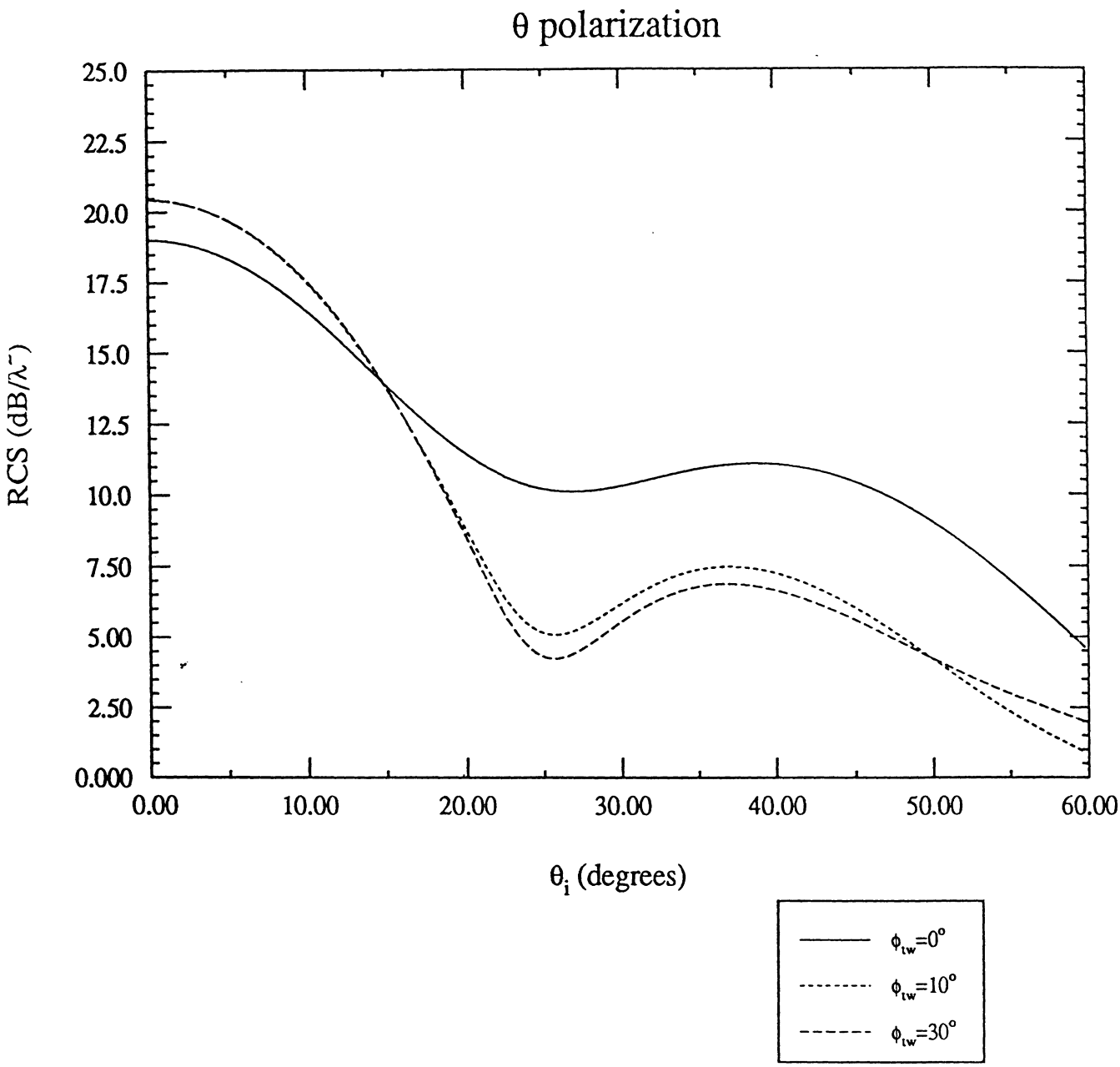

Figure 3: RCS (dB/λ^2) calculated by the G.T.E. - M. M. technique for a curved blade termination with $a = 0.5\lambda, b = \lambda, l_1 = 5\lambda, l_2 = \lambda$, 4 fins, $\phi_1 = 0^o$. (θ polarization).

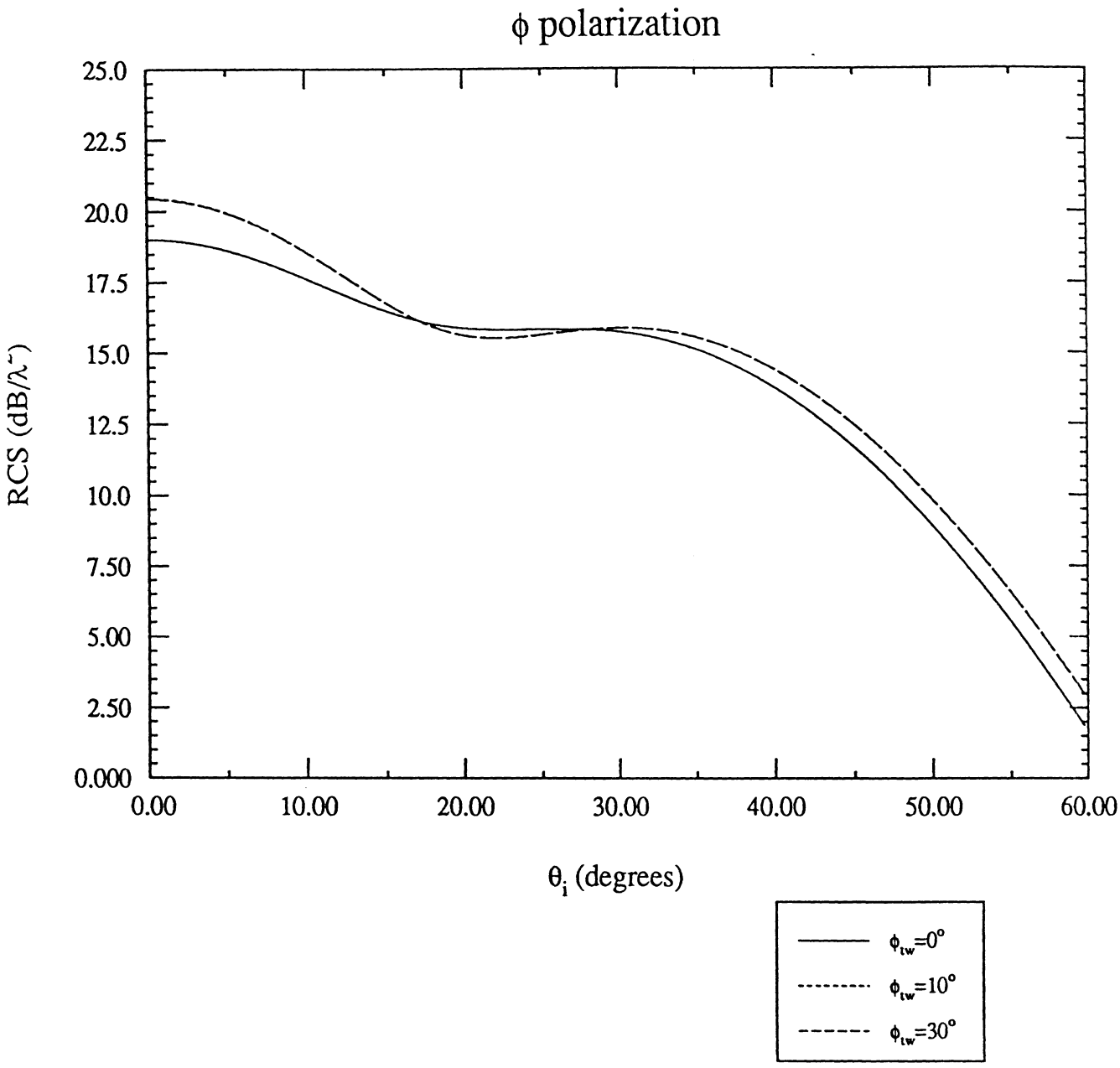

Figure 4: RCS (dB/λ^2) calculated by the G.T.E. - M. M. technique for a curved blade termination with $a = 0.5\lambda, b = \lambda, l_1 = 5\lambda, l_2 = \lambda, 4$ fins, $\phi_1 = 0^o$. (ϕ polarization).

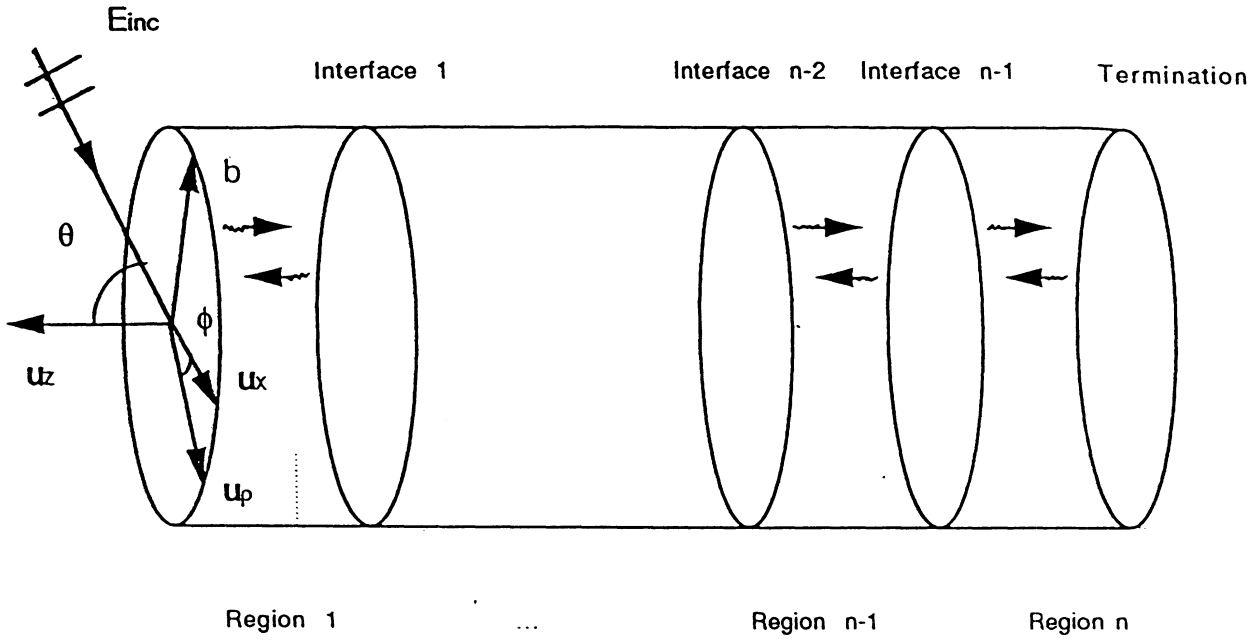

Figure 5: Illustration of a cavity with multiple sections having different propagation characteristics.

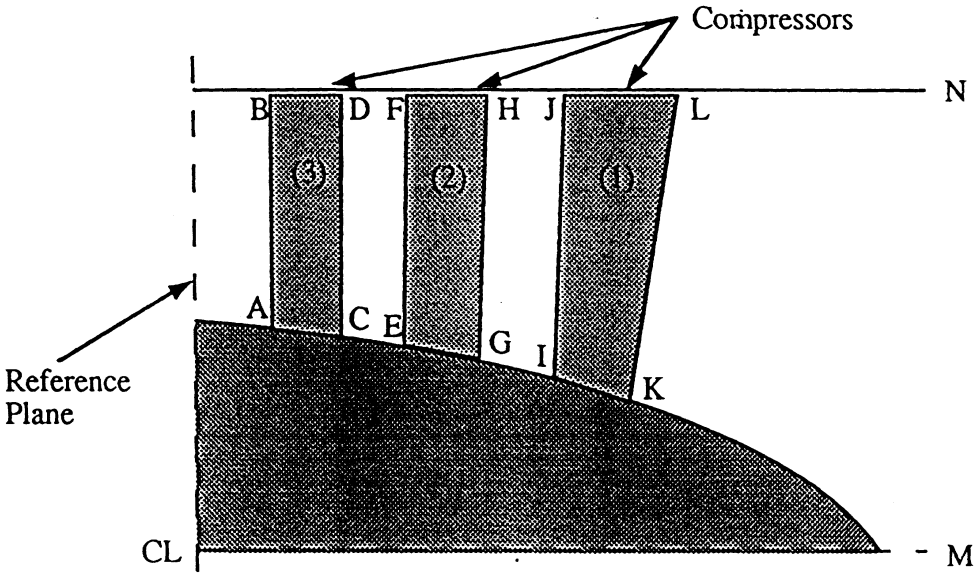

Blade Row (1); Inlet vanes; 17 blades
Blade Row (2); Compressor rotor; 20 blades
Blade Row (3); Compressor stator; 44 blades

Point	A	B	C	D	E	F	G	H	I	J	K	L	M	N
Axial	.90	.90	2.35	2.55	2.45	2.95	4.95	4.55	5.30	5.45	8.30	9.70	11.75	12.1
Diameter	9.15	13.30	8.20	13.30	8.10	13.25	5.00	13.15	4.75	13.40	2.80	13.80	-	13.8

All dimensions are in inches.

Figure 6: Some dimensions of the GO1 model.

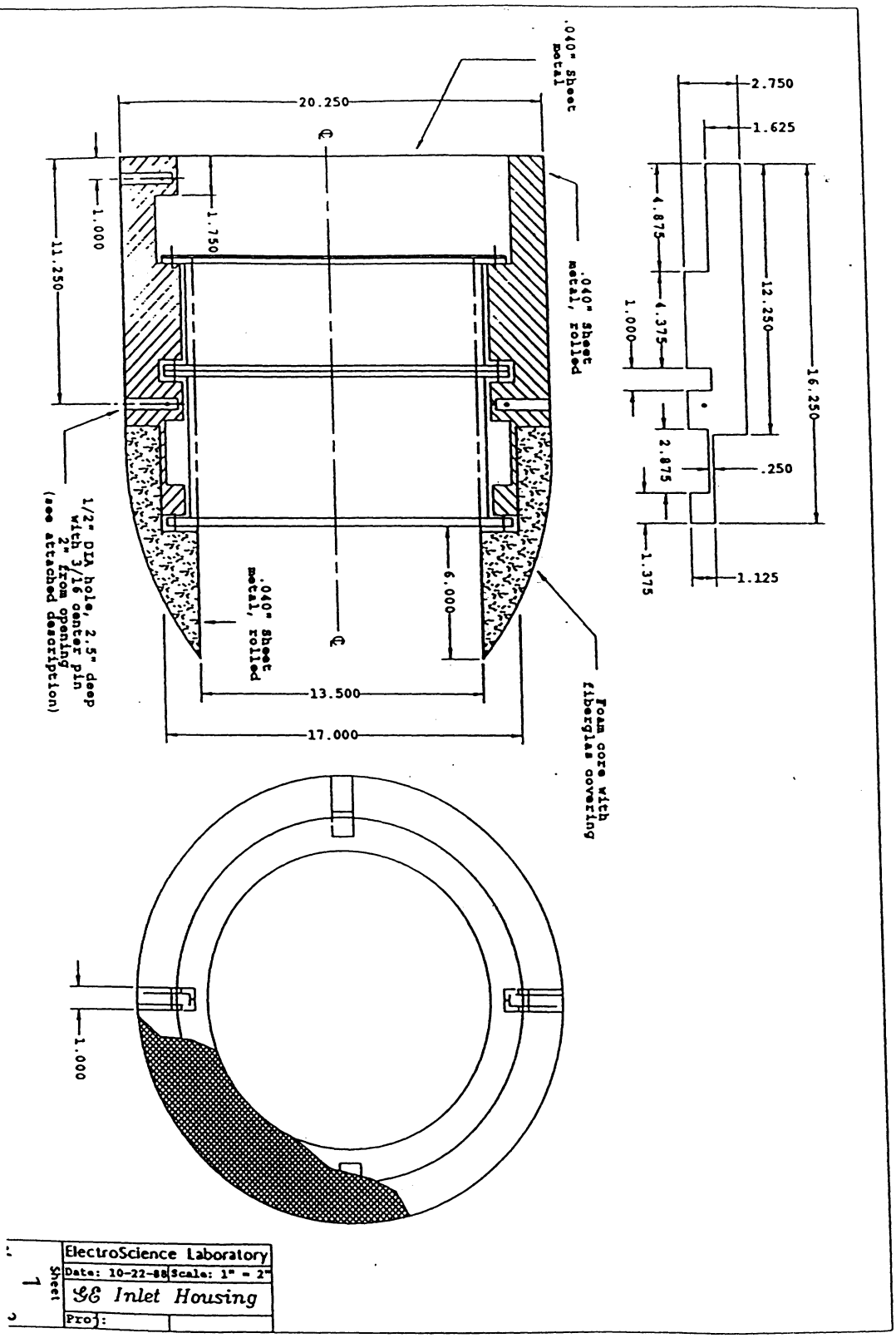

Figure 7: The short version of the GO1 measurement configuration.

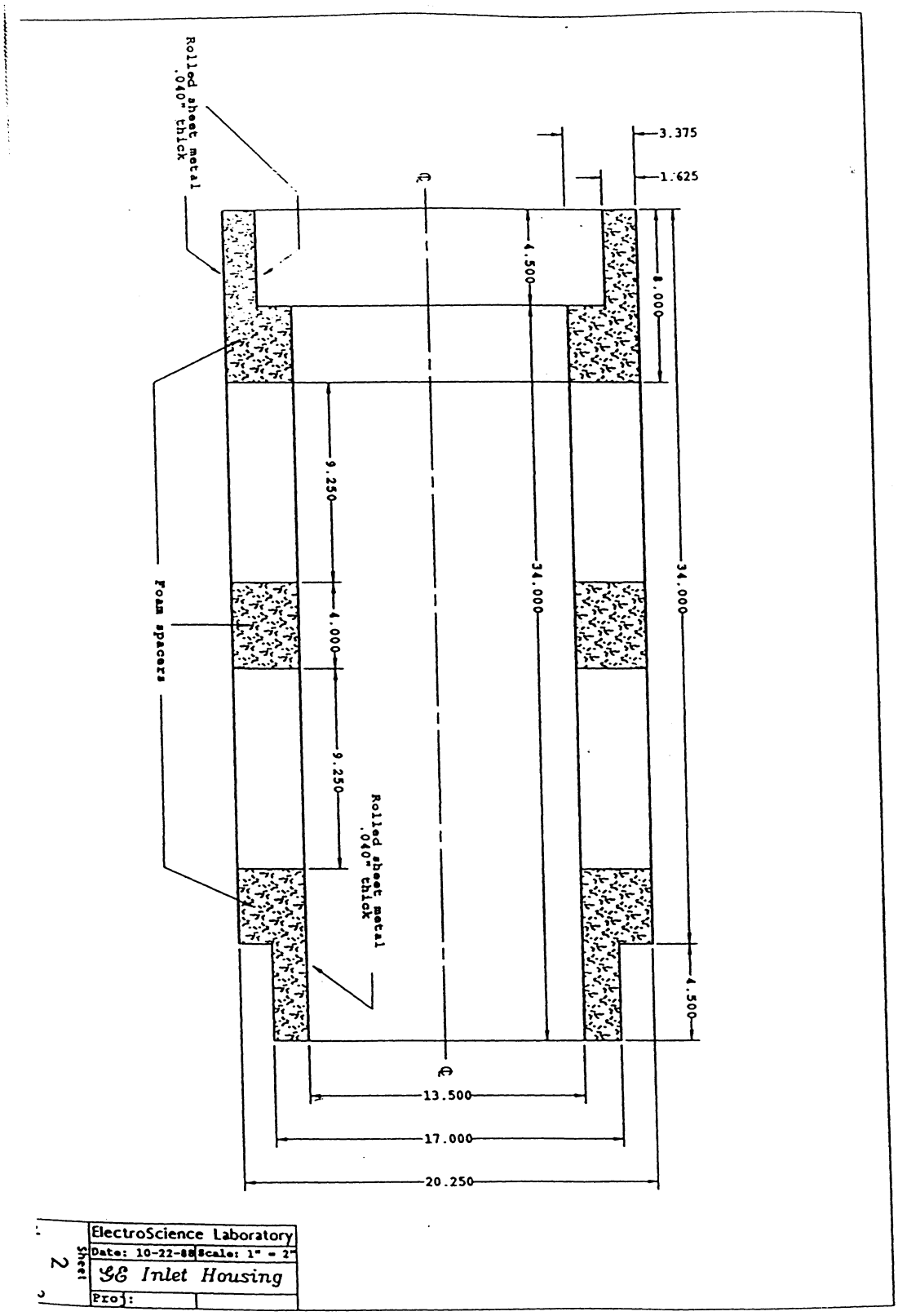

Figure 8: The duct inserted between the engine and the inlet to construct the long version of the GO1 measurement configuration.

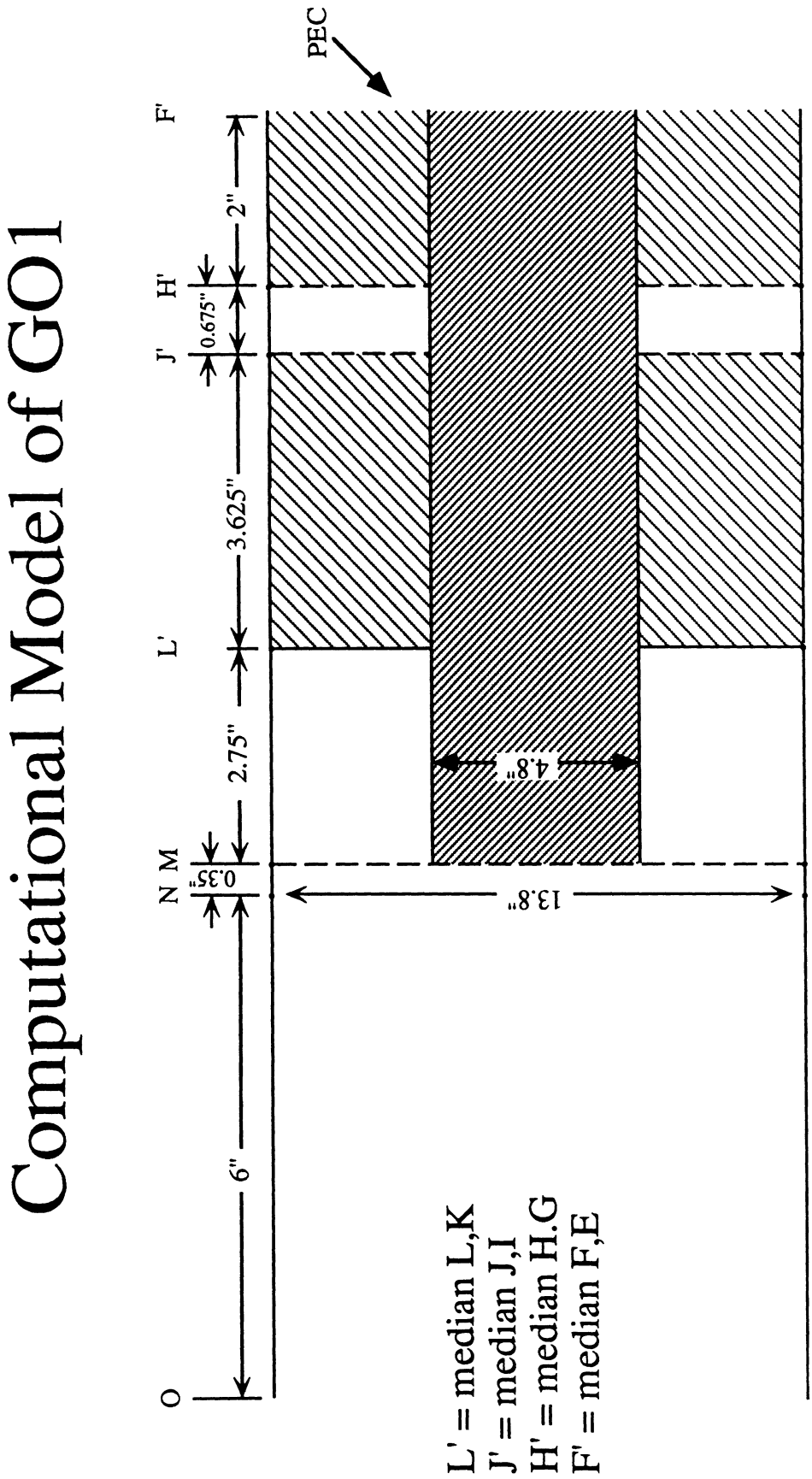

Figure 9: Computational model of the GO1 (2 stages).

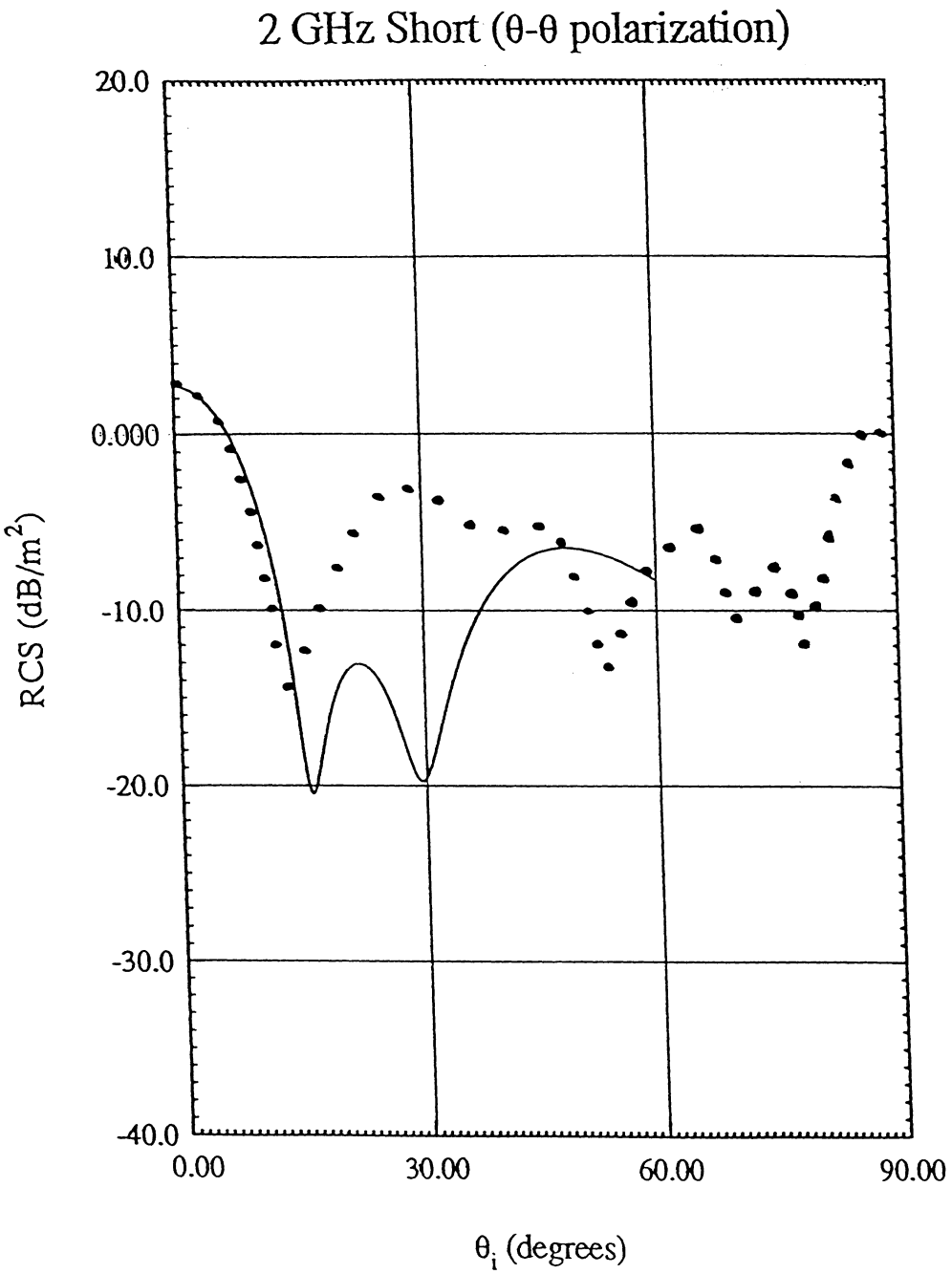

Figure 10. Comparison between numerical results (solid line) and measurements (dotted line) for the GO1 short inlet model (2 GHz, θ polarization).

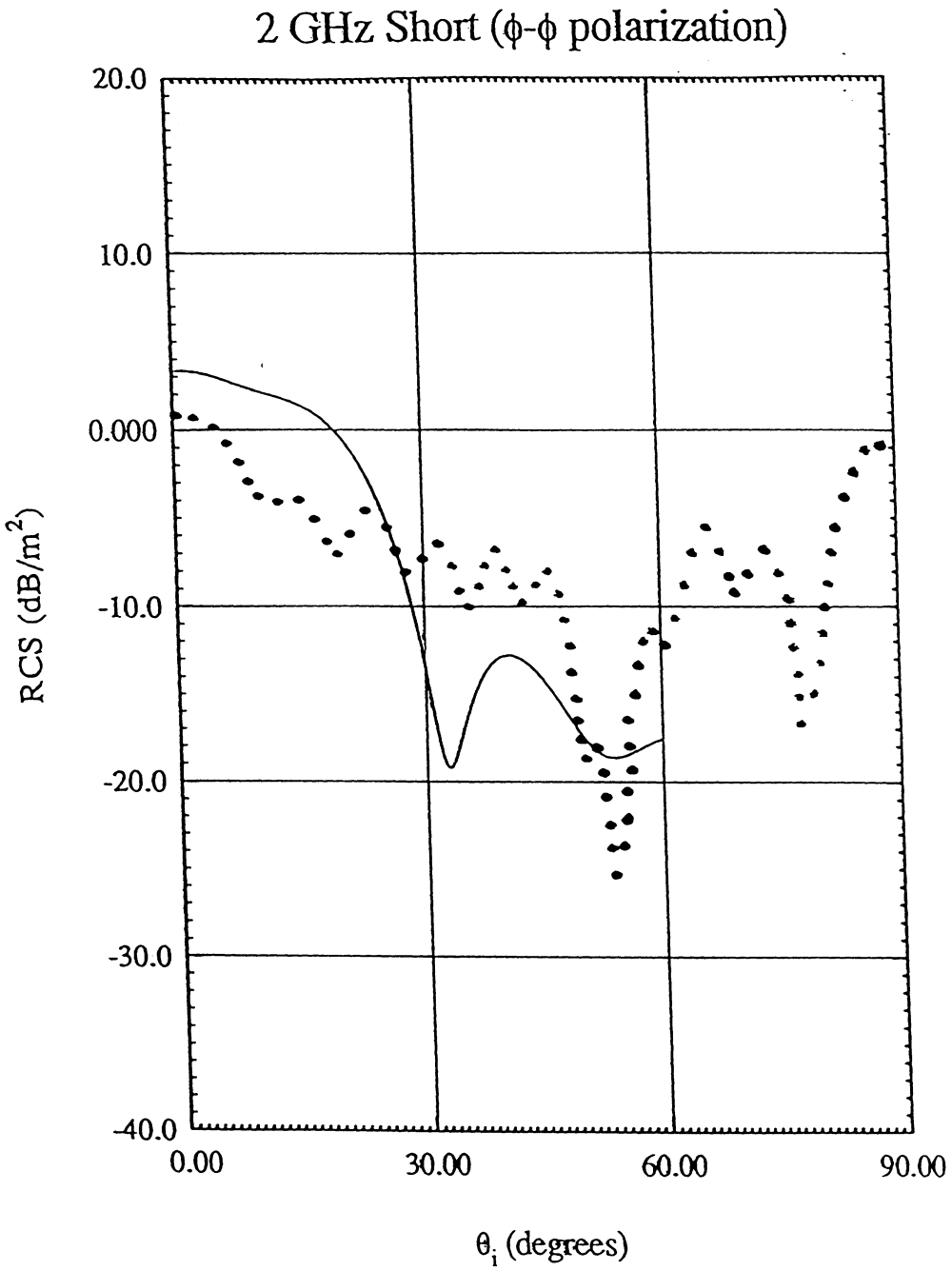

Figure 11. Comparison between numerical results (solid line) and measurements (dotted line) for the GO1 short inlet model (2 GHz, ϕ polarization).

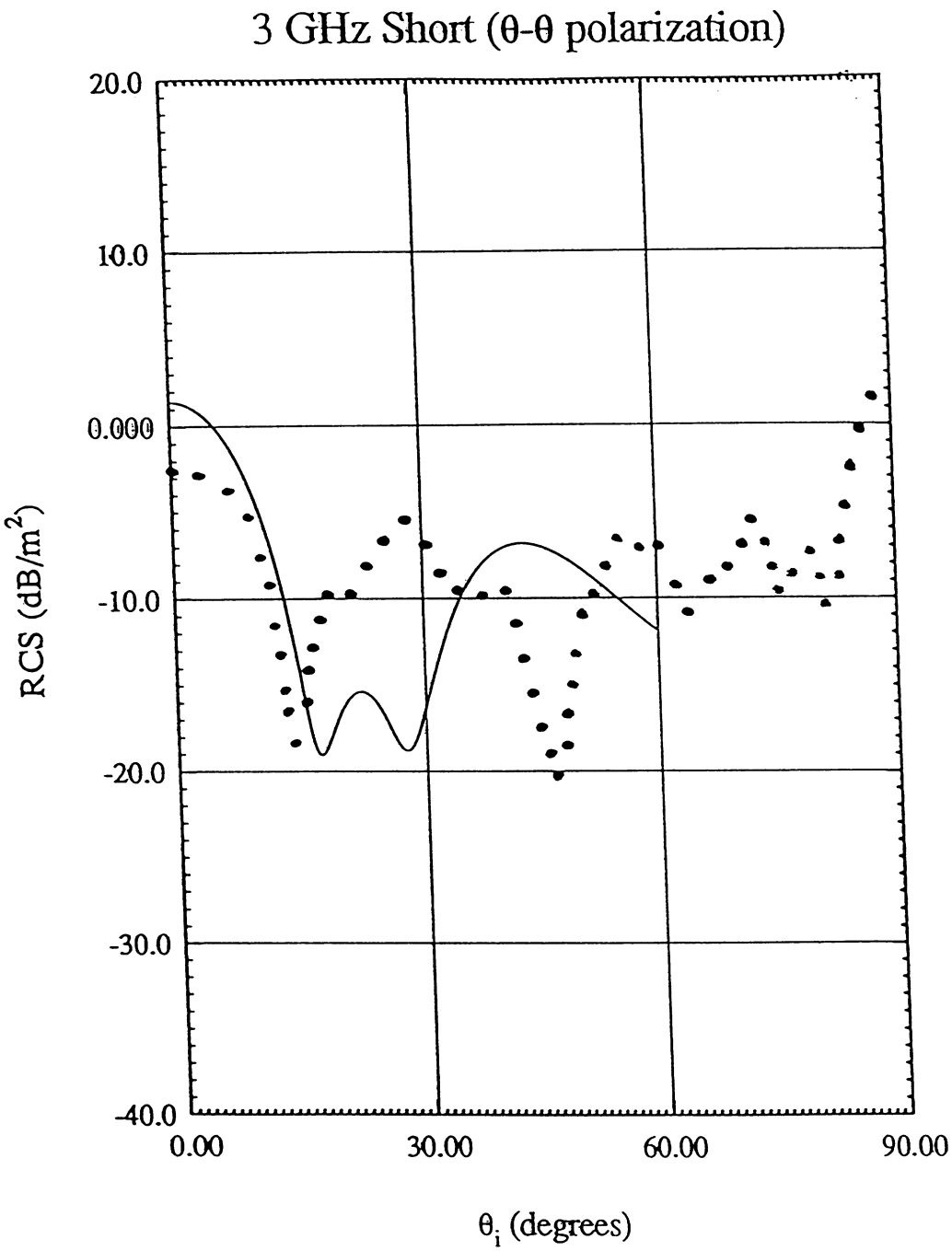

Figure 12. Comparison between numerical results (solid line) and measurements (dotted line) for the GO1 short inlet model (3 GHz, θ polarization).

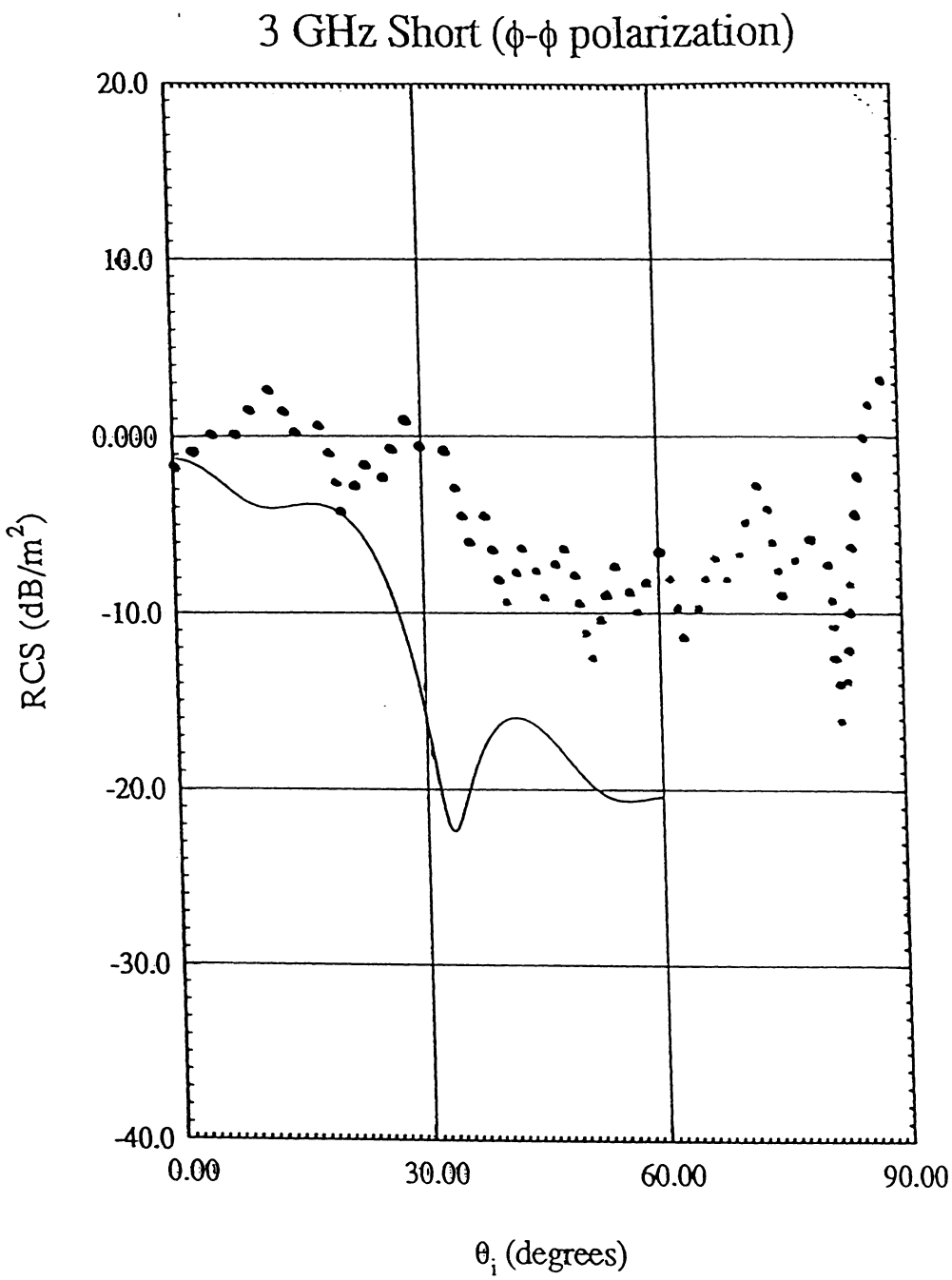

Figure 13. Comparison between numerical results (solid line) and measurements (dotted line) for the GO1 short inlet model (3 GHz, ϕ polarization).

Overlapping Modal and Geometric Symmetries in the Simulation of Jet Engine Inlet Scattering

Daniel C. Ross, John L. Volakis and Hristos T. Anastassiu

Radiation Laboratory
University of Michigan
Ann Arbor MI 48109-2122

***abstract* -- By examining the solution for the scattering from a cylindrical inlet terminated by a fan-like structure possessing discrete angular symmetry, it is found that only a very limited amount of inter-modal coupling can possibly occur. By exploiting this fact in a hybrid finite element/modal scheme, a very efficient solution is developed where only one sector of the geometry need be considered. It is shown that a phase boundary condition at the interior walls of the mesh is sufficient for the complete solution of the problem. The implementation of this phase boundary condition is detailed for the full three-dimensional case and important numerical considerations are given which if overlooked can lead to an illconditioned system. A simple example is shown for the hybrid finite element/modal scheme to validate the method.**

1.0 Introduction

The use of a hybrid finite element/modal technique to model the radar scattering from jet engine inlets was described in [1]. In brief, the finite element method (FEM) was used to generate a modal scattering matrix for the engine face while some high frequency or mode technique was used to trace the fields in and out of the inlet. It is necessary to perform the FEM analysis once for each traveling mode in the inlet.

While the method was validated in [1] for an engine-like termination consisting of straight blades, the electrical sizes considered were small (approximately 1λ radius) with respect to a realistic situation where the inlet can have a radius of 10λ and greater. To apply the method directly to such large structures would invoke computational costs that are indeed staggering. Consider that the number of elements (and number of degrees of freedom) in the mesh must grow as the radius squared. Also, the number of traveling modes (analysis must be done repeated for each mode) and the size of the scattering matrix, grow as the radius squared. For the inlet configurations considered in [1] approximately 50,000 elements were needed with about 20,000 degrees of freedom and the analysis was repeated approximately 10 times, once for each mode. Given this, an inlet 10λ in radius would require 100 times the computational resources (5,000,000 elements) and the analysis would need to be done 100 times over (2,000,000 degrees of freedom, 1,000 times), thus, increasing the total computational cost by about 10,000. In effect, the computational cost must increase as the radius to the fourth power.

Obviously, some physically derived simplification is needed to scale the problem to a workable size. Given the cyclic, geometric symmetry which exists in an engine face, it will be shown that it is possible to reduce the entire problem down to that of a single unique slice of the geometry. For example, if the engine face has 40 blades, then the FEM analysis need be carried out for only a single sector with encompasses one 40'th of the total volume.

Computational scaling can only be done for modal field excitations and not for arbitrary excitations. This is because to achieve scaling, both the angular symmetry of the modes, and the geometric symmetry are exploited. Of course, once the modal scattering matrix is created, any field which is incident on the mouth of the inlet can be decomposed into its modal constituents and the scattering pattern found. The combination of the modal and geometric symmetries gives rise to a very limited set of possible scattered modes and it turns out that all of these possible scattered modes have equal phase shift across the width of one slice. This physical sifting of the modes by the engine face is similar to the discrete spectrum of frequencies that are present in the Fourier Transform of a periodic signal. From a computational point of view, since the scattered modes all have equal phase shift across the slice, a phase boundary condition can be imposed at the two interior faces of the FEM mesh to bound the problem. This technique has been used successfully in [2] and [3] and is extended to 3-dimensions in this report.

Section 2.0 of this report justifies the scaling of the problem to one slice by showing that the overlapping modal and geometric symmetries give rise to a limited set of scattered/reflected modes and furthermore these modes can be modeled with a phase boundary condition on the interior walls of the mesh for a single slice of the whole geometry.Section 3.0 shows the implementation of the phase boundary conditions for the full three-dimensional problem including some impor-

tant numerical considerations that if overlooked can lead to an illconditioned system. Section 4.0 shows results for the hybrid finite element/modal analysis making full use of the overlapping modal and geometric symmetries. The last section introduces a new 'limited mode method' for approximating the scattering from potentially large inlet structures. This method uses the proceeding analysis to justify the use of a very simple and efficient scheme that is shown to predict the scattering from a relatively complex inlet/engine configuration with surprising accuracy.

2.0 Overlapping Modal and Geometric Symmetries

Although in [1] it was convenient to use cylindrical waveguide modes whose angular dependance was either $\cos(n\phi)$ or $\sin(n\phi)$, in order to exploit the symmetry of the engine face, the modes must now be defined as having $e^{\pm jn\phi}$ dependance. It is the angular phase shift across a sector that will make it possible to exploit the geometric symmetry.

Consider an engine-like termination as shown in Figure 2. Let ϕ_s be the angular extent of the unique slice of the geometry. For any fan-like structure $\phi_s = \frac{2\pi}{N_s}$ where N_s is the symmetry number (number of blades.) Since the incident field will be a cylindrical mode with angular dependance of $e^{\pm jn_{in}\phi}$, the boundary conditions that will be imposed on each slice will be the same but with a progressive phase shift of $e^{\pm jn_{in}\phi_s}$. That is, the FEM system resulting from a solution of the entire problem would take the form

$$\begin{bmatrix} K^1 & & & & \\ & K^2 & & & \\ & & K^3 & & \\ & & & \cdots & \\ & & & & K^{N_s} \end{bmatrix} \begin{pmatrix} E_s^1 \\ E_s^2 \\ E_s^3 \\ \cdots \\ E_s^{N_s} \end{pmatrix} = \begin{pmatrix} f \\ fe^{\pm jn_{in}\phi_s} \\ fe^{\pm 2jn_{in}\phi_s} \\ \cdots \\ fe^{\pm(N_s-1)jn_{in}\phi_s} \end{pmatrix} \tag{1}$$

where E_s^k is the unknown scattered electric field in slice k. Because the geometry is the same in each slice, $K^1 = K^2 = K^3 \ldots = K^{N_s}$ and the unknown scattered fields must all be equal to within a phase factor. That is

$$
\begin{aligned}
E_s^2 &= E_s^1 e^{\pm j n_{in} \phi_s} \\
E_s^3 &= E_s^1 e^{\pm j 2 n_{in} \phi_s} \\
&\cdots \\
E_s^{N_s} &= E_s^1 e^{\pm j (N_s - 1) n_{in} \phi_s}
\end{aligned}
\tag{2}
$$

and consequently, the scattered field is a periodic function in ϕ with period ϕ_s and a progressive phase advance of $e^{\pm j n_{in} \phi_s}$ in each period (slice.) To find which scattered modes can make up such a field, we consider the Fourier Transform of such a function where the variables ϕ and n_{out} are a Fourier Transform pair. That is, by examining the spectral content of a signal which is periodic in ϕ, but with a progressive phase advance $e^{\pm j n_{in} \phi_s}$, the set of possible outgoing modes n_{out}'s can be found.

Consider a signal $S(\phi)$ which is periodic but with a progressive phase advance.

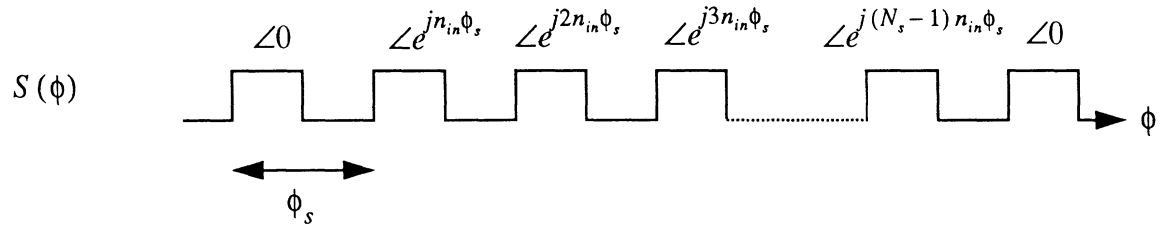

This signal can be considered to be a sum of N_s signals, each with an angular offset and a phase shift from a reference signal $S_0(\phi)$ where

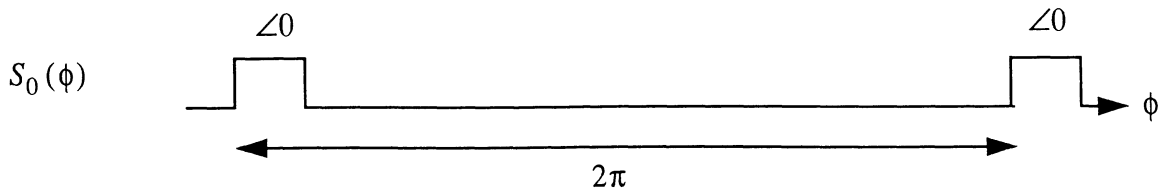

Mathematically, we have

$$
S(\phi) = \sum_{k=0}^{N_s - 1} S_0(\phi + k\phi_s)\, e^{j k n_{in} \phi_s}
\tag{3}
$$

and the Fourier Transform ($\phi \leftrightarrow n_{out}$) of such a signal can be found directly using the properties of shifting and linearity to give

$$\tilde{S}(n_{out}) = \tilde{S}_0(n_{out}) \sum_{k=0}^{N_s-1} e^{jk(n_{in}-n_{out})\phi_s} \tag{4}$$

Examination of the sum in (4) reveals that only if

$$n_{out} = n_{in} \pm mN_s \qquad m\text{: any integer} \tag{5}$$

is this sum nonzero. Thus the spectrum of $S(\phi)$ is made up of a limited set of modes, given by (5).

The implication of (5) are that for a given N_s (number of blades), only certain scattered modes can exist for a given incident mode. For example, if there are 17 blades and the incident mode is associated with $n_{in} = 1$, then only scattered modes which have $n_{out} = 1, 18, -16, 35, -33\ldots$ can exist. For $n_{in} = 2$ only scattered modes with $n_{out} = 2, 19, -15, 36, -32\ldots$ will be present in the scattered field. With this property in mind, it is worthwhile to consider if any additional physical insights can be gained into this complex scattering problem.

First we discuss the physical insights that can be gained due to the limited mode property. For an inlet termination with axial symmetry (a body of revolution, such as a circular stub, a cone, a bulb etc.) the symmetry number N_s goes to infinity. Thus only coupling as $n_{out} = n_{in}$ can occur. This is consistent with what is known from classical body of revolution theory. An important practical implication of (5) is that as the number of blades increases, the higher order scattered modes will be pushed up farther. Coupling to these higher order modes will become impossible if the modes are highly evanescent. However, even if these higher order modes do propagate, they will be of such a radically different nature so that coupling must again be very weak. Thus, for structures with many blades the dominant scattered modes have an index of $n_{out} = n_{in}$.

An important result is that coupling does not occur to modes having $n_{out} = n_{in} \pm 1$ since a symmetry number of 1 is physically impossible. This fact will turn out to be of great importance for establishing boundary conditions on the axis of the FEM solution. To consider more of the effect of the limited mode property on the FEM solution, note that all of the possible scattered modes share a common phase shift from symmetry face 1 to symmetry face 2, (see Figure 2.) Thus, all scattered modes are related, on a cut of constant z, from face 2 to face 1 by

$$\begin{aligned} E_\rho^2 &= E_\rho^1 e^{\pm jn_{in}\phi_s} \\ E_\phi^2 &= E_\phi^1 e^{\pm jn_{in}\phi_s} \\ E_z^2 &= E_z^1 e^{\pm jn_{in}\phi_s} \end{aligned} \tag{6}$$

where E^2 is the field on face 2 and E^1 is the field on face 1. This fact was first exploited in [2] to efficiently compute eigenmodes within a cyclotron using FEM. For the jet engine scattering problem then, a phase boundary condition can be used to bound the FEM solution region to only one slice of the original problem. The implementation of the phase boundary condition for three-dimensional FEM analysis of the engine face is explored next.

3.0 Phase Boundary Conditions for 3-D FEM

In the previous section it was shown that the only condition needed to relate the fields on the two symmetry faces is a phase boundary condition, given by (6). The implementation of this condition is complicated because it must be enforced over a a surface which includes the axis. The implementation of phase boundary conditions on the axis cannot be avoiding because of the presence of a material absorber designed to absorb modal fields. Also, the phase boundary conditions enforce the cylindrical components of the field while the FEM solution is in terms of the cartesian components.

The FEM mesh which is generated to model the slice must have coincident nodes and elements on the two symmetry faces. Therefore for each degree of freedom on face 2 (E_x^2,E_y^2, E_z^2), there is a corresponding degree of freedom on face 1 (E_x^2,E_y^2, E_z^2). During assembly of the FEM system, degrees of freedom on face 2 can be discarded in favor of degrees of freedom on face 1 by enforcing the phase boundary condition as

$$
\begin{aligned}
E_x^2 &= \frac{\left[\rho_x^1 - \rho_y^2\left(\frac{\phi_x^1}{\phi_y^2}\right)\right] e^{\pm j n_{in}\phi_s} E_x^1 + \left[\rho_y^1 - \rho_y^2\left(\frac{\phi_y^1}{\phi_y^2}\right)\right] e^{\pm j n_{in}\phi_s} E_y^1}{\rho_x^2 - \rho_y^2\left(\frac{\phi_x^2}{\phi_y^2}\right)} \\
E_y^2 &= \frac{\left[\phi_x^1 - \phi_x^2\left(\frac{\rho_x^1}{\rho_x^2}\right)\right] e^{\pm j n_{in}\phi_s} E_x^1 + \left[\phi_y^1 - \phi_x^2\left(\frac{\rho_y^1}{\rho_x^2}\right)\right] e^{\pm j n_{in}\phi_s} E_y^1}{\phi_y^2 - \phi_x^2\left(\frac{\rho_y^2}{\rho_x^2}\right)} \\
E_z^2 &= e^{\pm j n_{in}\phi_s} E_z^1
\end{aligned}
\tag{7}
$$

where $\rho^1_{(x,y,z)}$, $\phi^1_{(x,y,z)}$ and $\rho^2_{(x,y,z)}$, $\phi^2_{(x,y,z)}$ are the components of the polar unit vectors at face 1 and 2 respectively.

The hybrid FEM-Modal formulation given in [1] makes use of a special broadband absorber designed to absorb outgoing cylindrical waveguide modes. This absorber was designed specifically for this problem because the standard finite element mesh truncation schemes were not found to be effective. Since this material absorber occupies part of the mesh and must be placed at some distance in front of the engine face, the space between the engine face and the absorber must include the axis of the guide. Consequently, some degrees of freedom are located on the axis and this fact introduces a complication to the slicing scheme not been previously encountered. While the transverse, polar field components cannot be defined on the axis, the transverse cartesian components can be defined. This fact is a motivation for leaving the finite element formulation in terms of cartesian components rather than polar components.

In practice, boundary conditions on the axis must be imposed differently for different modal excitations. By considering the field behavior along the axis, and the limited mode coupling effect, a consistent set of boundary conditions can be applied along the axis. First, consider the behavior of the modes on the axis as shown in Table 1. As was previously observed, it is impossible for mode coupling to occur as $n_{out} = n_{in} \pm 1$, so there will never be a mode from column 1 and column 2 present simultaneously. If a column 1 mode can be present then the boundary conditions on the axis are enforced as $E_x = E_y = 0$. If a mode from column 2 can be present then the boundary condition $E_z = 0$ is enforced. If all scattered modes are such that $n_{out} > 1$ then the conditions $E_x = E_y = E = 0$ are imposed.

TABLE 1. Behavior of modes on axis

	n=0	n=1	n>1
TE E_x, E_y	= 0	max.	= 0
TE E_z	= 0	= 0	= 0
TM E_x, E_y	= 0	max.	= 0
TM E_z	max.	= 0	= 0

Careful implementation of boundary conditions on conductors was neccessary so as to preserve the condition of the system, and similar issues relating to the implementation of the phase boundary conditions will be outlined next. In [1] a simple procedure for enforcing the boundary conditions on a conductor in an optimum way was given. This procedure however cannot be used at the

point where a conductor crosses one of the symmetry faces. The boundary conditions on a conductor that crosses a symmetry face must be enforced so that during assembly, both the phase boundary condition and the metal boundary conditioned are enforced. This can be accomplished with the following procedure which is performed at the element level.

Given that a node lies on a conductor with normal $\hat{n}$ and on symmetry face 1:

- if $|\hat{\phi} \times \hat{n}| > 0.15$ then set $\hat{t}_1 = \dfrac{\hat{\phi} \times \hat{n}}{|\hat{\phi} \times \hat{n}|}$

  else set $\hat{t}_1 = \dfrac{\hat{\rho} \times \hat{n}}{|\hat{\rho} \times \hat{n}|}$

- $\hat{t}_2 = \dfrac{\hat{z} \times \hat{t}_1}{|\hat{z} \times \hat{t}_1|}$

- Given the three local equations for E_x^s, E_y^s and E_z^s at the node

  - find the largest component of $\hat{t}_1$ (x, y or z) and replace the corresponding equation in the element system with $\hat{t}_1 \cdot \bar{E}^s = -\hat{t}_1 \cdot \bar{E}^{inc}$

  - find the largest component of $\hat{t}_2$ (x, y or z) and replace the corresponding equation in the element system with $\hat{t}_2 \cdot \bar{E}^s = -\hat{t}_2 \cdot \bar{E}^{inc}$

For a node that lies on a conductor and on symmetry face 2, the procedure is the same except that the largest component of the tangent vectors ($\hat{t}_1$ and $\hat{t}_2$) must be found for the corresponding node on face 1 and the local equations replaced accordingly. In this way, when (7) is used for assembly, both boundary conditions (face 1 and face 2) will be enforced correctly and the condition of the system will be preserved. It is noted however that if the slice angle ϕ_s approaches 90 degrees, the formulation breaks down as the boundary conditions on face 1 and face 2 become orthogonal and cannot be enforced simultaneously and this can be seen by inspection of (7). This is not considered an important limitation since real jet engine faces always have many more than four blades.

4.0 Hybrid Modal/FEM Example

The advantages in using the overlapping symmetries becomes apparent as soon as the task of mesh generation is undertaken. Only a fraction of the mesh for the entire structure is needed, and the importance of this cannot be over stressed. With the level of sophistication currently built into the FEM software, it is required that the mesh on symmetry faces 1 and 2 be coincident so only a limited number of geometries can be analyzed: axial symmetric structures and straight blades. In order to model curved blade structures, it will be necessary to impose the phase boundary condition across dissimilar mesh areas. This can be done by interpolating degrees of freedom on face 2 to a linear combination of degrees of freedom on face 1.

As an example, a short terminated inlet with radius of 0.66λ is analyzed by using only a 4 degree slice of the original problem. The absorber is place 0.5λ from the short. In this case, any size slice is sufficient, but a balance was achieved by considering that if the slice is too thin, more elements will be needed as the element size must shrink to fill the narrow slice. While this geometry is in

fact a body of revolution, it is a very important benchmark for validating the correct implementation of the phase boundary conditions, which is indeed quite a complex task. The calculated scattered fields for two important modal excitations are shown in Figure 3 and Figure 4. The fields calculated by the FEM are seen to have the correct modal behavior for a reflected mode from a short.

5.0 Conclusions and Future Work

The physically derived phenomenon of limited mode coupling has been derived and shown to be of use for scaling the hybrid FEM-modal solution for the jet engine inlet problem. Considerations were made for the fact that the axis is included in the solution domain and important numerical considerations for the proper implementation of the phase boundary conditions for 3-dimensional FEM were given. The phase boundary conditions were shown to accurately predict the modal fields scattered from a shorted inlet using only a 4 degree slice of the actual problem.

The method is currently being applied to straight blade structures and the method needs to be extended to handle terminations with curved blades since the analysis of curved blades requires the enforcement of the phase boundary condition across dissimilar mesh areas. An interpolation from degrees of freedom on face 2 to degrees of freedom on face 1 must be done, making the enforcement of the phase boundary conditions more complex.

As an outcome of this research, the possibility of creating a very simple and efficient 'limited mode model' can be introduced. The limited mode model gives a physically justifiable reason why the scattering matrix must be very sparse for terminations with many blades. Preliminary studies show that even with a first order 'limited mode model', fairly accurate predictions of the patterns from complex structures can be made. A first order model involves no modal coupling and assumes that each mode simply reflects from a different location on the termination. The scattering matrix can therefore be created very simply and efficiently even for large complex structures. Currently, studies are being done on the proper way to find the reflection points for each modes and it is hoped that sufficiently accurate predictions can be made with this model so that large, realistic structures can be analyzed in the near future.

Monostatic RCS

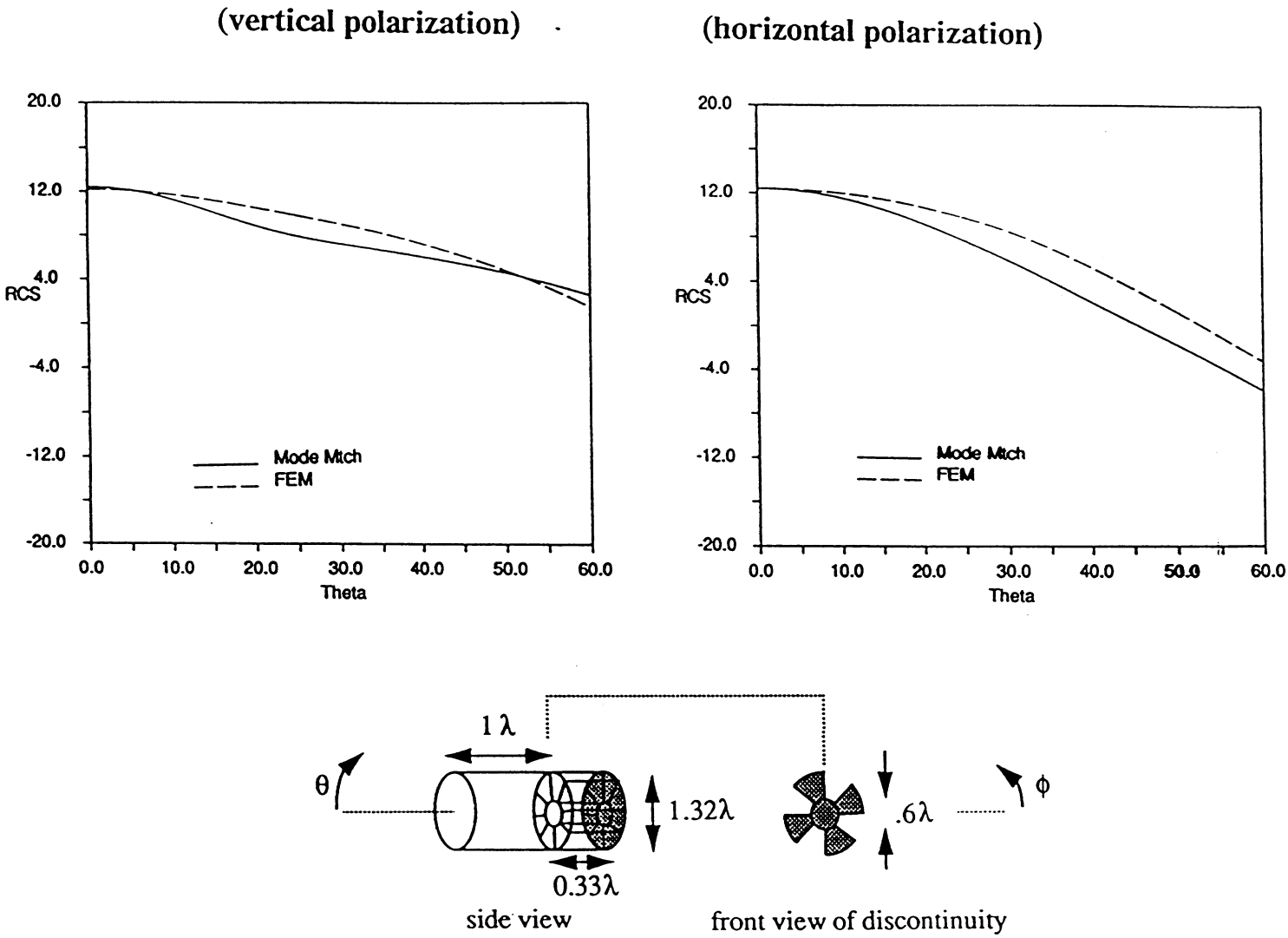

FIGURE 1. An inlet terminated in a ridged structure.

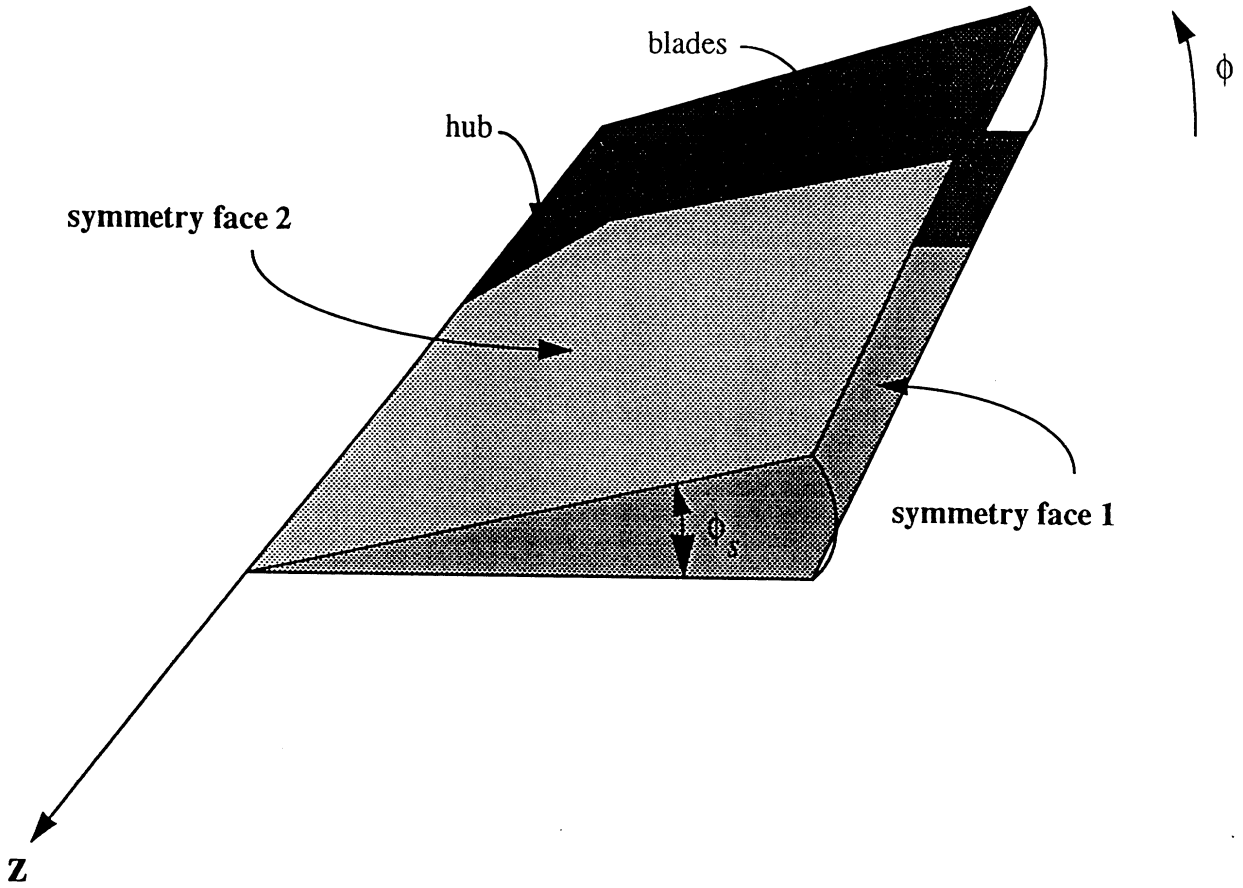

FIGURE 2. A unique slice of an engine-like termination.

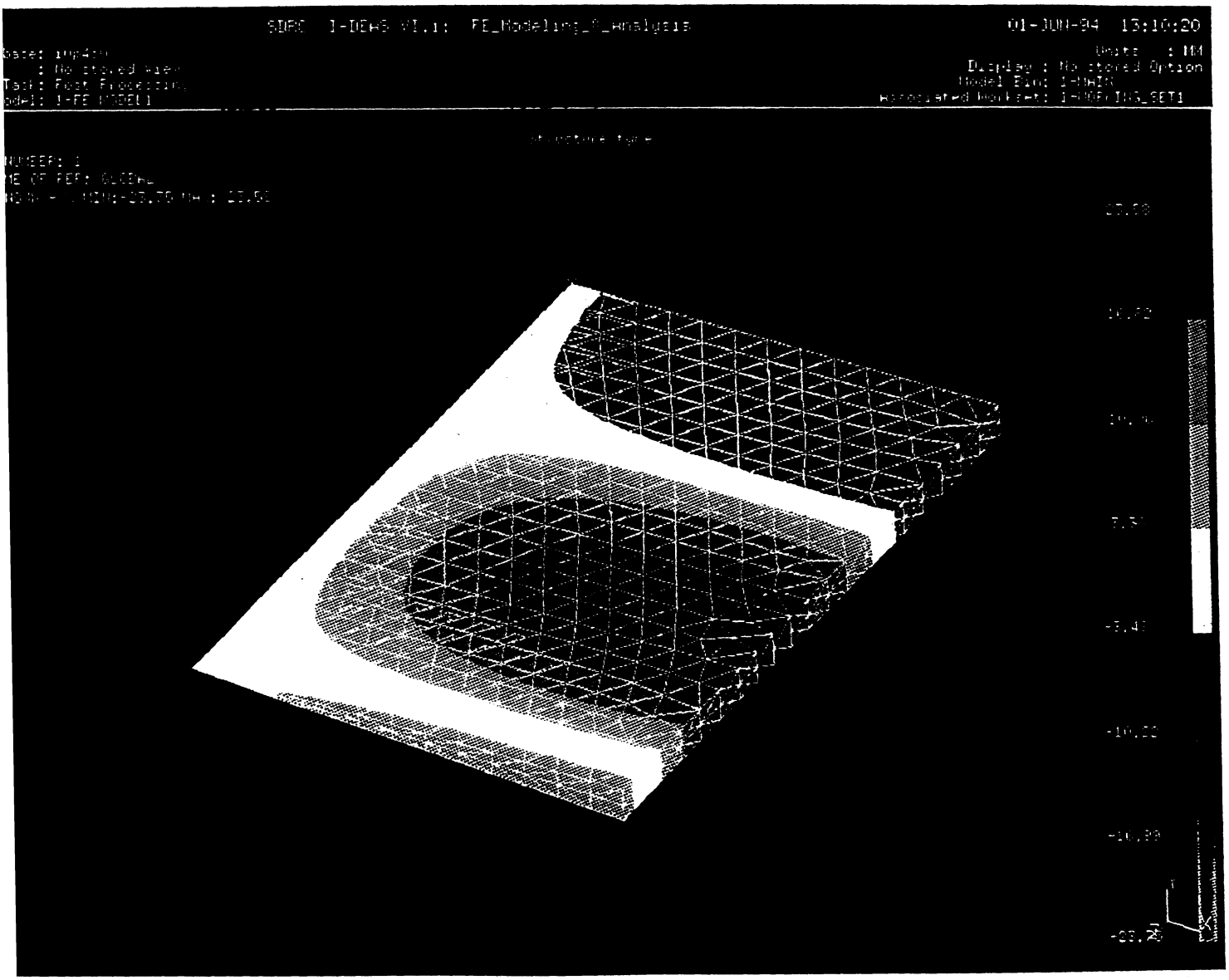

FIGURE 3. Calculated scattered field $Re\,(E_\rho)$ for TM_{01} excitation of a shorted inlet using a four degree slice.

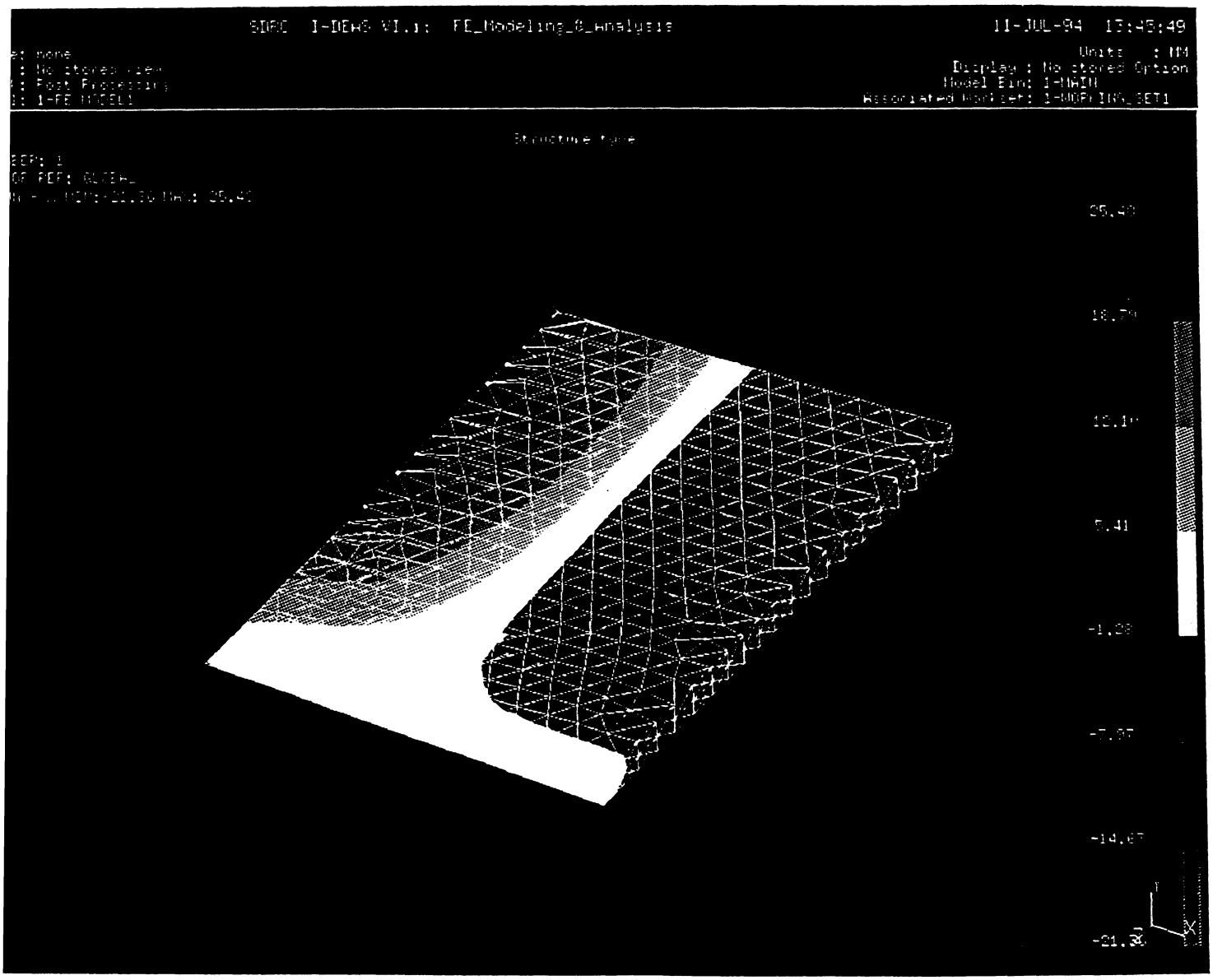

FIGURE 4. Calculated scattered field ($Re\ (E_\rho)$)for TE_{11} excitation of a shorted inlet using a four degree slice

REFERENCES

[1] D.C. Ross, J.L. Volakis and H.T. Anastassiu, "Hybrid Finite Element-Modal Analysis of Jet Engine Inlet Scattering", Technical Report 030395-4-T, The University of Michigan, EECS Radiation Laboratory, Ann Arbor MI, January, 1994.

[2] E.M. Nelson, "High Accuracy Electromagnetic Field Solvers for Cylindrical Waveguides and Axisymmetric Structures Using the Finite Element Method", Ph.D. dissertation, Stanford University, Stanford, CA, 1993; also SLAC-431

[3] A. Frenkel, J.R. Brauer and M.A. Gockel, "Complex Periodic Boundary Conditions for AC Finite Element Models", *Proceedings of the 10th Annual ACES Conference*, 1994, pp. 195-202.